J. Mech. Phys. Solids 169 (2022) 105067

Contents lists available at ScienceDirect

Journal of the Mechanics and Physics of Solids

journal homepage: www.elsevier.com/locate/jmps

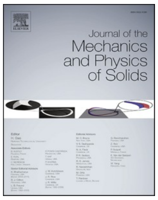

Hierarchical multiscale crystal plasticity framework for plasticity and strain hardening of multi-principal element alloys

Qihong Fang[a], Weizheng Lu[a], Yang Chen[a], Hui Feng[a], Peter K Liaw[b], Jia Li[a,*]

[a] *State Key Laboratory of Advanced Design and Manufacturing for Vehicle Body, College of Mechanical and Vehicle Engineering, Hunan University; Changsha 410082, PR China*
[b] *Department of Materials Science and Engineering, The University of Tennessee, Knoxville, TN 37996, USA*

ARTICLE INFO

Keywords:
Hierarchical multiscale model
Crystal plasticity finite element
Discrete dislocation dynamics
Multi-principal element alloy
Strain hardening

ABSTRACT

The multi-principal element alloys (MPEAs) exhibit the unprecedented combinations of the excellent mechanical properties, especially high strength and good ductility. However, the accurate and reasonable models for describing the mechanical behavior of MPEAs are still scarce due to their distinctive serious lattice distortion effects, which limit the performance prediction. Here, we develop a new general framework by combining the atomic simulation, discrete dislocation dynamics, and crystal plasticity finite element method, to study the strain-hardening behavior for MPEAs, which achieves the influence of the complex cross-scale factors, including the lattice distortion at the nanoscale and the dislocation hardening at the microscale, on the plastic deformation. Compared with the classic crystal plasticity finite element, the bottom-up hierarchical multiscale model could couple the underlying physical mechanisms from the nano-micron-meso scales and captures the inhomogeneous strain field induced by the serious lattice distortion, thus showing the high accuracy and ubiquitous availability for MPEAs. The result shows that the prediction of the strain-stress curve in the polycrystal MPEAs agrees well with the experimental result at the quasi-static tension, which verifies the accuracy of the proposed method. In addition to the dislocation evolution, the heterogeneous strain distribution combined with the significant change from the orientation of some grains could be an important reason for the enhanced strength at the micron scale. The present work not only gives an insight into the relationship between the multiscale microstructure and strain hardening considering the mechanistic linkages of the lattice distortion, dislocation behavior, and grain structure, but also provides a general approach to physically predict the mesoscopic mechanical response in MPEAs.

1. Introduction

In comparison with the traditional alloys, the multi-principal element alloys (MPEAs) composed by the multiple elements in near-equiatomic or equiatomic proportions (Yeh et al., 2004; Cantor et al., 2004), show the excellent performance, including the good fatigue resistance, high yielding strength, corrosion resistance, high ductility, and thermal stability (Hemphill et al., 2012; Zhang et al., 2014; Shi et al., 2017; Miracle and Senkov, 2017; Thurston et al., 2017; Shukla et al., 2018; Li et al., 2020; Pan et al., 2021; Shi et al., 2021; Fang et al., 2021; Zhang, et al., 2022). Therefore, the MPEAs are expected to be widely used in the key structural and functional

---

* Corresponding author.
E-mail address: lijia123@hnu.edu.cn (J. Li).

https://doi.org/10.1016/j.jmps.2022.105067
Received 27 March 2022; Received in revised form 3 September 2022; Accepted 12 September 2022

applications, such as the damage-resistant materials and tool materials, which have attracted the significant attentions (Otto et al., 2013; Gludovatz et al., 2014; Li et al., 2018; Fang et al., 2019; Bahramyan et al., 2020; Li et al., 2020; Peng et al., 2021). The experiments and simulations (Joseph et al., 2017;Fang et al., 2019; Xiao et al.,2019; Smith et al., 2020; Peng et al., 2021) show that different atomic types in MPEAs result in the large atomic lattice distortion to control the mechanical properties (Wang et al., 2018), different from the traditional alloys.

Recent numerical simulations reveal the deformation mechanisms of MPEAs from the nanoscale to microscale. For example, molecular dynamics (MD) simulations provide a powerful tool to deeply understand the plastic deformation of the MPEA at the nanoscale (Li et al., 2020). The dislocation-dislocation interaction, dislocation-solid solution interaction, deformation twinning and detwinning in the AlFeCrNiCu MPEA under the uniaxial tensile loading are systematically studied by MD simulations (Li et al., 2016). The solidification behavior of the Al_xCoCrFeNiCu MPEA from 2200 K to 300 K and their compressive behaviors after the solidification are explored, revealing the change of lattice distortion with the increasing Al content by MD simulations (Bahramyan et al., 2020). The operation mechanisms of the Frank-Read sources in MPEAs are explored at the microscale using the phase field dislocation dynamics simulation, revealing their strong size dependences (Smith et al., 2020). The discrete dislocation dynamics (DDD) can capture the dynamic evolution of a large number of dislocations at the microscale, and reveals the microscale mechanism of the dislocation-mediated plasticity (Arsenlis et al., 2006; Zhang et al., 2021). At the mesoscale, a crystal plastic finite element (CPFE) method can consider the various meso deformation mechanisms, such as the phase transition, dislocation slip and deformation twinning (Roters et al., 2019), and it has an obvious advantage for describing the plastic behavior of materials based on the microstructure evolution. A crystal plasticity model is developed to describe the cyclic plasticity of the MPEA (Lu et al., 2020). The modeling method of the solid-dissolution induced back-stress model is verified in a non-equiatomic MPEA using a finite element method (Kim et al., 2022). It is worth noting that the parameters of the crystal plasticity constitutive model are usually achieved by fitting the macroscopic experimental results (Deka et al., 2006). Unfortunately, the fitting parameters may not be unique, and thus reduce prediction accuracy of the CPFE simulation due to the lack of the submicron deformation mechanism (Chandra et al., 2018). Since the microstructures of MPEAs are multiscale, such as atomic vacancies and lattice distortion, microscale dislocations, and mesoscale grains, we need to consider the microscale deformation mechanism to obtain the exact parameters of the crystal plasticity constitutive model, and then develop a new simulation method integrated from the nano-micro-meso-scale microstructures.

The strengthening mechanism and the plastic deformation behavior in crystalline materials come from the complex interactions among the dislocations, solid solutions, grain boundaries, precipitation, and other defects (Essmann and Mughrabi, 1979; Kalidindi et al., 2001; Zhang et al., 2008; Li et al., 2016, 2020). Most of these phenomena are coupled at different scales, and the deformation behavior at the small scales determines the mechanical response of materials at the large scales (McGinty and McDowell, 2004). For example, the significant work has been done to unveil the multiscale relationship among the atomic lattice distortion, nanoscale precipitation, microscale dislocation behavior, and mesoscale mechanical property (Liang et al., 2018; Ding et al., 2019; Zhang et al., 2021). Therefore, developing a new model that crosses the time and length scales to solve this multiscale issue is necessary. There are two types of models, namely a parallel multiscale model and a hierarchical multiscale model. In the first kind of the parallel multiscale model, the simulation regions around the studied key regions (such as precipitates and cracks) uses detailed atomic simulations, and the continuity method is applied in the edge region. Scholars have developed many parallel multiscale models with various coupling modes, boundary conditions and simulation tools (Shenoy et al., 1998; Ortiz and Phillips, 1998; Wang et al., 2001; Shilkrot et al., 2002; Miller et al., 2004; Kulkarni et al., 2008; Davydov et al., 2014; Kim et al., 2014). Although this kind of model can calculate the plastic deformation from multiple-scale microstructures at the same time, the interface coupling between the regions contained the nano-micro-meso-scale microstructures still faces the major challenges. (Fish et al., 1997; Jarvis et al., 2001; Kouznetsova et al., 2002; Massart et al., 2007; Ghosh et al., 2009). Hierarchical-multiscale models include the asymptotic homogenization method (Fish et al., 1997; Massart et al., 2007; Ghosh et al., 2007), self-consistent framework (Zecevic and Knezevic, 2018), distribution-enhanced homogenization method (Alleman et al., 2015), and nonlinear homogenization method based on the varied fable principles (Song and Castañeda, 2018). Recently, the parametric homogenization-constitutive model was developed for multiscale modeling of deformation in the titanium alloy (Ozturk et al., 2019; Kotha et al., 2020; Ozturk et al., 2021).

The hierarchical multiscale models avoid the spurious wave reflections in the connection region caused by the direct coupling different scales, and thus have more extensive applications and powerful functions (Ozturk et al., 2019). At the atomic scale, the elastic constants, lattice constants, thermal expansion coefficients, and dislocation properties (including the dislocation mobility, Peierls stress, and Burgers vector) can be extracted from MD simulations as the input for the microscale simulation, which has been widely used (Po et al., 2016; Cho et al., 2016; Yin et al., 2021). Then, the results from the microscale DDD simulation are used to quantify the hardening parameters in the mesoscale CPFE constitutive equation (Groh et al., 2009; Chandra et al., 2015), for obtaining the hardening parameters of the single crystal material at the grain level. Since the polycrystalline materials are composed of the countless-randomly orientation grains, we need to calibrate the hardening parameters of a polycrystalline-constitutive model using the hardening parameters of the single crystal material. However, it is a severe challenge. The mechanical response of the polycrystalline is employing an appropriate Taylor factor calculated from the average of the single crystal response oriented at [100] and [111] (Hansen and Huang, 1998), but this method lacks the physical mechanisms. The potential hardening parameter of a representative volume element (RVE) in a polycrystalline material is calibrated using the simple average of a single-crystal response with [001], [111], [101], and [123] orientations (Renner et al., 2016), to reveal the deformation response of the FCC polycrystal Ni. However, the predicted results are not accurate due to the existence of the localized plastic strains (Renner et al.,2016). Therefore, a various oriented single-crystal response needs to be included to adequately calibrate the hardening parameters of the polycrystal RVE. More recently, the selected seven crystal orientations covering the standard stereographic triangle have successfully captured the mechanical response of a polycrystal copper during the uniaxial tension (Chandra et al., 2018).

The strengthening mechanisms considered by the various hierarchical multiscale models mentioned above (Groh et al., 2009; Chandra et al., 2015, 2018) are the dislocation strengthening. However, compared with the traditional alloys, MPEAs produce particularly extraordinary lattice distortions due to the differences in the atomic size and shear modulus between the different principal elements. Due to the local stress field caused by the severe lattice distortion in MPEAs strongly hinders the dislocation movement, the previous hierarchical multiscale-modeling approach without considering lattice-distortion effects is difficult to apply to explore the plastic behavior of MPEAs.

In this study, a hierarchical multiscale approach that can capture the severe lattice distortion in MPEAs is proposed by coupling with the MD, DDD, CPFE simulation methods and the random-field theory (Fig. 1), for modeling MPEAs, and this approach connects three length scales (nanoscale, microscale, and mesoscale). Among the studied MPEA systems, the AlxFeCoCrNi MPEA has been extensively studied due to its excellent specific strength, radiation resistance, and low-temperature mechanical properties (Zhang et al., 2014; Miracle and Senkov, 2017; Wang et al., 2012). Here, the FCC $Al_{0.1}$FeCoCrNi MPEA is used as the model alloy in our work. The mechanical response of the polycrystal RVE at different strain rates is investigated using a proposed method in a model of $Al_{0.1}$FeCoCrNi MPEA. The elastic constants and the single dislocation motion information of MPEAs extracted by the nanoscale MD simulations are integrated into higher scale DDD simulations. The stress field caused by lattice distortion is introduced in the microscale DDD simulations using the random-field theory. Then, we establish DDD simulations with various crystal orientations (including [001], [011], [111], [102], [112], [212], and [213], which covers the standard stereotaxic triangle) because the $Al_{0.1}$FeCoCrNi MPEA is simulated to obtain the hardening parameters of the crystal plasticity model. At the mesoscale, we predict the mechanical response of the single crystals with 7 crystal orientations, and calibrate the hardening parameters of polycrystals using the hardening parameters of 7 orientated single crystals. The rationality and accuracy of the proposed multiscale method are verified by comparing the predicted mechanical response with the experimental observations (Wu et al., 2017; Jiang et al., 2020) of uniaxial tension of the polycrystal $Al_{0.1}$FeCoCrNi MPEA at different strain rates. We analyzed the pole figures and the distribution of stress and strain in the polycrystal $Al_{0.1}$FeCoCrNi MPEA at various plasticity strains under different strain rates.

2. Hierarchical multiscale crystal plasticity framework

2.1. Molecular dynamics

Molecular dynamics is mainly based on the classical Newtonian mechanics and Hamiltonian equation. The total energy of a system containing N atoms is the sum of the kinetic energy and potential energy of every atom in the system, which can be expressed as follows

$$U_{total} = U_{ke} + U_{pe} = \sum_{i=1}^{n} \left(U_{ke,i} + U_{pe,i} \right) \tag{1}$$

where U_{ke} and U_{pe} are the kinetic energy and potential energy of the system, respectively. $U_{ke,i}$ and $U_{pe,i}$ are the kinetic energy and potential energy of the atom i, respectively.

The force on an atom, i, in the system is the gradient of the potential energy

$$\vec{F}_i = -\nabla_i U_{pe} = -\left(\vec{i}\frac{\partial}{\partial x_i} + \vec{j}\frac{\partial}{\partial y_i} + \vec{k}\frac{\partial}{\partial z_i} \right) U_{pe} \tag{2}$$

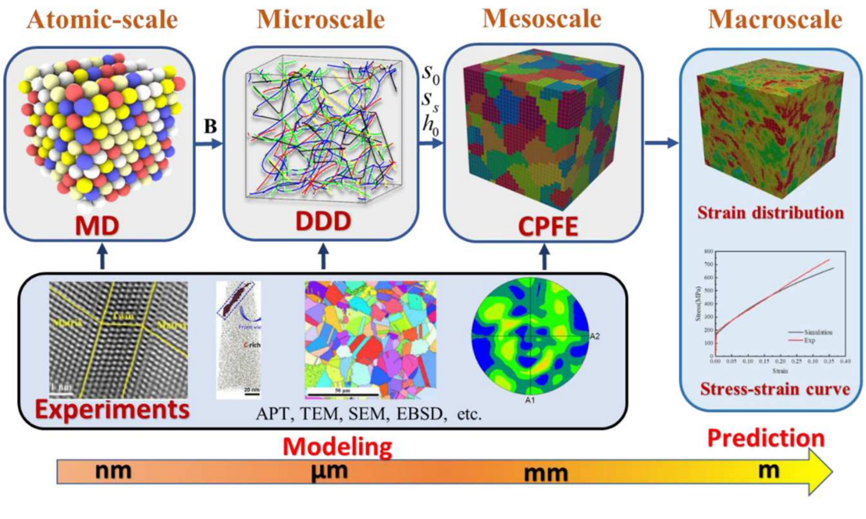

Fig. 1. A hierarchical multiscale-modeling strategy to estimate the hardening parameters in the crystal plasticity constitutive model. The coupled models of MD, DDD, and CPFE to predict the mechanical response of the polycrystalline materials at different length scales.

Here, $\overrightarrow{F}_i = m_i\overrightarrow{a_i}$. Thus, the dynamics of atoms obeys the Newton's law.

2.2. Discrete dislocation dynamics

The dislocation line in the DDD simulation is discretized into some dislocation segments, which is limited by nodes. The force acting upon these nodes, F_i^{node}, can be obtained by superimposing the contributions of all dislocation segments connecting this node, i:

$$F_i^{node} = \sum_j f_{ij} \tag{3}$$

where the segment force, f_{ij}, is obtained by a line integral:

$$f_{ij} = \int_{C_j} N_i^j(s) f_{ij}^{\mathrm{PK}}(s) dL(s) \tag{4}$$

Here, C_j represents the segment, ij. $N_i^j(s) = s$ $(0 \le s \le 1)$ is an interpolation function, and s is the location index. For example, the positions specified by $s = 0$, 0.5, and 1 are the node, j, the midpoint of the segment, ij, and the node, i, respectively. The Peach–Koeler force, $f_{ij}^{\mathrm{PK}}(s)$, at the position, s, is dependent on the local stress, $\sigma(s)$:

$$f_{ij}^{PK}(s) = \left[\sigma^{ext}(s) + \sigma^{disl}(s) + \sigma^{mpea}(s)\right] \bullet \mathbf{b} \times \mathbf{t}_{ij} \tag{5}$$

where $\sigma^{ext}(s)$ is the external load stress, and $\sigma^{disl}(s)$ is the stress from other dislocations. $\sigma^{mpea}(s)$ is the stress induced by the atomic lattice distortion in the MPEAs which is calculated by a fractal function, as presented in the next section. $\widehat{t}_{ij}$ is the unit vector parallel to a dislocation line, and b_{ij} is the Burgers vector of the segment, ij. Once the force on the node, i, is known, the velocity of the node, i, is given by the kinetic law:

$$v_i = F_i^{node} / B \tag{6}$$

where B is a viscous drag coefficient.

The cross-slip process dominated by an energy barrier relies on the Escaig stress (Kuykendall et al., 2020), and depends on the local stress, $\sigma(s)$. Based on the Arrhenius-type law, the cross-slip rate is:

$$\mathrm{R} = v_0 \exp\left(-\frac{E_b}{K_{\mathrm{B}}T}\right) \tag{7}$$

where K_B is the Boltzmann's constant, T is the temperature, and $v_0 = v_D(L/L_0)$ is the attempt frequency. v_D is the Debye frequency, L is the length of a screw dislocation segment, and $L_0 = 1$ μm stands for a reference length. The energy barrier can be expressed as

$$E_b = E_a - V_a \Delta\tau_E \tag{8}$$

where $E_a = 0.4$eV is the energy required to form a constriction point on the screw dislocation (Hussein et al., 2015; Rao et al., 2017), $V_a = 20b^3$ is the activation volume (Hussein et al., 2015), and $\Delta\tau_E$ is the difference between the Escaig stresses on the primary and cross-slip planes.

Therefore, the dislocation velocity is calculated by Eq. (6) under an external stress. Accordance to the Orowan's law, the plastic shear strain from that a dislocation segment with Burgers vector, b_n, glides a distance, δ, on a slip plane, A_n, can be written as:

$$\delta\gamma_n^p = \frac{b_n \delta A_n}{V} \tag{9}$$

The overall macroscopic plastic-strain rate tensor can be calculated as:

$$\delta\dot{\varepsilon}_{ij} = \sum_{\alpha=1}^{12} \frac{1}{2}\left(n_i^{(\alpha)} \otimes b_j^{(\alpha)} + b_j^{(\alpha)} \otimes n_i^{(\alpha)}\right)\delta\dot{\gamma}^{(\alpha)} \tag{10}$$

where $n_i^{(\alpha)}$ is the unit normal vector of a slip plane, α, and $b_j^{(\alpha)}$ is the Burgers vector. The velocity of a single dislocation calculated by MD simulations is introduced into the DDD simulation to obtain the strain-hardening behavior caused by the large-scale collective dislocation movement in the single crystals, which provides material-hardening parameters for the crystal plasticity model.

2.3. Crystal plasticity

The constitutive behavior of the $\mathrm{Al_{0.1}FeCoCrNi}$ MPEA is illuminated by a crystal plasticity framework to capture the slip-based plastic deformation of the polycrystalline materials. The crystal plasticity model is originally developed by the previous work (Kalidindi et al., 1992). For the completeness, the partial key ingredients can be presented, and thus the detailed content concerning theoretical equations and numerical implementation of the crystal plasticity are not specified. The more details are discussed in the references (Kalidindi et al., 1992; Anand et al., 1996; Yaghoobi et al., 2019).

The plastic deformation is accommodated across slip on the specified slip systems. Accordingly, the total deformation gradient tensor, **F**, and the macroscopic velocity gradient tensor, **L**, can be decomposed into the elastic and plastic components, respectively,

$$\mathbf{F}=\mathbf{F}^{\mathbf{e}}\mathbf{F}^{\mathbf{p}};\quad \mathbf{L}=\mathbf{L}^{\mathbf{e}}+\mathbf{L}^{\mathbf{p}} \tag{11}$$

where $\mathbf{F}^{\mathbf{e}}$ represents the rigid body rotation and the elastic distortion of the crystal lattice, and $\mathbf{F}^{\mathbf{p}}$stands for the glide of dislocations on the active slip systems. The plastic part of the macroscopic velocity gradient, $\mathbf{L}^{\mathbf{p}}$, is given as the sum of the shearing rates on all slip systems:

$$\mathbf{L}^{\mathbf{p}}=\dot{\mathbf{F}}_{\mathbf{p}}\mathbf{F}_{\mathbf{p}}^{-1}=\sum_{\alpha=1}^{N}\dot{\gamma}^{\alpha}\mathbf{m}_0^{\alpha}\otimes\mathbf{n}_0^{\alpha} \tag{12}$$

where $\mathbf{m}_0^{\alpha}$ is the slip direction, $\mathbf{n}_0^{\alpha}$ is the slip plane normal, and $\dot{\gamma}^{\alpha}$ is the plastic shearing rate on the α^{th} slip system ($\dot{\gamma}^{\alpha}>0$). The integer, α, is the crystal-slip system for 12 slip systems in FCC materials. The Cauchy-Green elastic strain tensor, $\mathbf{E}^{e}$, is related to the deformation gradient acting on the intermediate configuration as

$$\mathbf{E}^{e}\equiv(1/2)\left(\mathbf{F}_e^{T}\mathbf{F}_e-\mathbf{I}\right),\quad \mathbf{T}\equiv\mathbb{C}\mathbf{E}^{e} \tag{13}$$

where $\mathbb{C}$ is the fourth-rank elasticity tensor. The resolved shear stress, τ, on $\alpha(\mathbf{m}_0^{\alpha},\mathbf{n}_0^{\alpha})$ slip system is expressed as

$$\tau=\left(\mathbf{F}_e^{T}\mathbf{F}_e\mathbf{T}\right)\cdot\mathbf{S}_0^{\alpha} \tag{14}$$

where $\mathbf{S}_0^{\alpha}=\mathbf{m}_0^{\alpha}\otimes\mathbf{n}_0^{\alpha}$ is the Schmid tensor. In the crystal plasticity theory, the evolution of the plastic strain rate in each slip system, $\dot{\gamma}^{\alpha}$, is adopted the strain-rate-sensitivity method (Asaro et al., 1985):

$$\dot{\gamma}^{\alpha}=\dot{\gamma}_0\left|\frac{\tau^{\alpha}}{\tau_{sr}^{\alpha}}\right|^{1/m}\mathrm{sign}(\tau^{\alpha}\Big) \tag{15}$$

where $\dot{\gamma}_0$ is the reference value of the slip rate, and represents the macroscopic plastic strain rate applied to the material. τ^{α} is the applied shear stress on the slip system, τ_{sr}^{α} (>0) is the slip-system-deformation resistance, and m is the strain rate sensitivity index of the slip. The resistance parameter, $\dot{\tau}_{sr}^{\alpha}$, of the α-slip system is in accordance with the following equation

$$\dot{\tau}_{sr}^{\alpha}=\sum_{\beta}\left|\dot{\gamma}^{\beta}\right|h^{\alpha\beta} \tag{16}$$

where $\dot{\gamma}^{\beta}$ quantifies the shear rate of each slip system. $h^{\alpha\beta}=[q_0+(1-q_0)\delta^{\alpha\beta}]h^{\beta}$is the hardening matrix, which describes both the latent hardening and self-hardening of the slip systems. $\delta^{\alpha\beta}$ is the Kronecker delta. The self-hardening parameter,h^{β}, is multiplied by the latent-hardening parameter,q_0, and constitutes the hardening matrix $h^{\alpha\beta}$. The self-hardening parameter is expressed as

$$h^{\beta}=h_0\left|1-\frac{\tau_{sr}^{\beta}}{s_s^{\beta}}\right|^{r^{\beta}} \tag{17}$$

where h_0 is the initial hardening parameter, r^{β} is the hardening exponent for the β-slip system, and s_s^{β} is the slip resistance at the hardening saturation for the β-slip system. The slip resistance parameters, including $\{h_0, s_0, s_s, r^{\beta}\}$, are assumed to be the same for all 12 slip systems and serve as the input parameters to the CPFE simulations (Sundararaghavan et al., 2008; Lu et al., 2020). According to the previous work (Li et al., 2013), the latent-hardening parameter and hardening exponent used in our CPFE simulations are q_0 =1.4 and $r=2.25$, respectively.

2.4. MD- and DDD- driven CPFE framework

In this section, we briefly introduce the transmission strategy of connecting nano-micron-meso-scale parameters in a multiscale modeling method. The single dislocation velocity and thermodynamic parameters (including the potential barrier and activation volume) of the MPEAs generated by the nanoscale MD simulation are transferred to the micronscale DDD simulations. Compared with the traditional alloys, the local stress fields caused by the severe lattice-distortion effect in MPEAs strongly hinder the dislocation movement and enhance the dislocation nucleation rate, improving the strength of materials. For the DDD simulations, the lattice-distortion effect for MPEAs is considered by embedding a three dimension (3D) lattice-strain field. The relevant parameters required for the flow and hardening rules of the above crystal plastic model need to be obtained from the micron scale DDD simulations.

The collective movement of a large number of dislocations causes the plastic hardening and deformation of materials. The dislocation hardening is related to the strengthening relationship predicted by the mathematical equation of the CPFE model. Therefore, we can couple the DDD results with the constitutive equation of the crystal-plasticity model.

The evolution of the plastic shearing strain rate, $\dot{\gamma}^{\alpha}$, of the CPFE model is specified by $\dot{\gamma}^{\alpha}=\dot{\gamma}_0|\frac{\tau^{\alpha}}{\tau_{sr}^{\alpha}}|^{1/m}\mathrm{sign}(\tau^{\alpha}\Big)$. Using the theory of a thermally-activated glide, $\dot{\gamma}_0$and the strain rate sensitivity, m, can be expressed as a function of temperature(Fivel et al., 1998)

$$\dot{\gamma}_0 = b^2 \rho_m v_d \exp\left(\frac{-\Delta Q_s}{kT}\right), \quad \text{and} m = \frac{k_B T}{\alpha b^2 \mu r_0} \tag{18}$$

where $\dot{\gamma}_0$ represents the macroscopic plastic strain rate imposed on the material, b is the Burgers vector magnitude, ρ_m is the mobile dislocation density, v_d is the average dislocation velocity, $k_B = 1.38 \times 10^{-23}\text{JK}^{-1}$is the Boltzmann constant, T is the temperature, α is the average forest strength, μ is the shear modulus, r_0 is the dislocation radius, and ΔQ_S is the activation energy for the slip. At room temperatures, r_0 is approximately 5b, and the strain rate sensitivity is 0.04. In addition, the hardening is more strongly affected by the temperature than the yielding stress in an FCC alloy (Li, 2008).

In the current work, the applied shear stress, τ^α, on the slip system can be decomposed into two components(Balasubramanian and Anand, 2002):

$$\tau^\alpha = \tau^\alpha_{thermal} + \tau^\alpha_p \tag{19}$$

where $\tau^\alpha_{thermal}$ and τ^α_p represent thermal and athermal components of the slip resistance during plastic deformation. In MPEAs, $\tau^\alpha_{thermal}$ is predominantly dominated by the solid solution strengthening and lattice friction effects (Jiao et al., 2018; Li et al., 2020), and τ^α_p is controlled by the interaction between dislocations. The solid solution strengthening in alloys is essentially the elastic interactions between the local stress fields formed by solute atoms and the dislocation. Compared with the traditional alloys and multi solute element alloys, MPEAs have particularly severe lattice distortion effects (Li et al., 2020). The local stress field from the severe lattice distortion in MPEAs strongly hinders the dislocation movement. The lattice distortion effect is considered in the DDD simulations by embedding a 3D lattice strain field for the CPFM simulation (The details are described in the next section).

Therefore, the flow rule, $\dot{\gamma}^\alpha = \dot{\gamma}_0 \left|\frac{\tau^\alpha}{\tau^\alpha_{sr}}\right|^{1/m} \text{sign}(\tau^\alpha\Big)$, can be rewritten as

$$\dot{\gamma}^\alpha = \dot{\gamma}_0 \left|\frac{\tau^\alpha_{thermal} + \tau^\alpha_p}{\tau^\alpha_{sr}}\right|^{1/m} \text{sign}(\tau^\alpha\Bigg) \tag{20}$$

where $\dot{\gamma}^\alpha$is obtained from the strain rate history computed by the DDD simulations. The constants ($\dot{\gamma}_0$, m) are determined by a priori based on the previous work (Li et al., 2008; Groh et al., 2009). The other parameters are depicted in the simulation setup for the next section.

It can be noted that τ^α and $\dot{\gamma}^\alpha$ are a function of time, which can be obtained by the DDD simulations. Now, only one unknown, τ^α_{sr}, in Eq. (20) evolves with the simulation time, as the deformation progresses. Hence, Eq. (20) is used to calculate the evolution of the total slip resistance, τ^α_{sr}, over time. Thus, the change rate of the total slip resistance can be quantified using DDD simulations during the deformation.

Based on Eqs. (16) and (17), when shearing on the β-slip system, the evolution process of the slip resistance of the α-slip system can be given:

$$\dot{\tau}^\alpha_{sr} = \sum_\beta |\dot{\gamma}^\beta| \left[q_0 + (1-q_0)\delta^{\alpha\beta}\right] h^\beta_0 \left|1 - \frac{\tau^\beta_{sr}}{s_s}\right|^{r^\beta} \tag{21}$$

In the DDD simulations, the plastic deformation caused by the dislocation slide must be balanced with the externally applied deformation. As the total plastic-strain rate of all slip systems is constant (Mecking et al., 1981; Groh et al., 2009; Chandra et al., 2018). In this manner, the evolution of the slip resistance of each slip system can be expressed as

$$\dot{\tau}^\alpha_{sr}(t) = \dot{\gamma} \sum_\beta \left[q_0 + (1-q_0)\delta^{\alpha\beta}\right] h^\beta_0 \left|1 - \frac{\tau^\beta_{sr}(t)}{s_s}\right|^r \tag{22}$$

where $\dot{\gamma} = \sum|\dot{\gamma}^\beta|$, $\dot{\tau}^\alpha_{sr}(t)$ is the change rate of the slip resistance on the α-slip system, and $\tau^\beta_{sr}(t)$ is the change rate of the slip resistance on the β-slip system with time. For each time node of the DDD simulations, 12 equations correspond to 12 slip systems, and each equation includes the same unknowns of h_0 and s_s. Then, a calibration program is built using the Newton-Raphson method, to determine the several hardening parameters.

For the α-slip system, the residual, d^α, can be calculated by:

$$d^\alpha(t) = \dot{\tau}^\alpha_{sr}(t) - \dot{\gamma} h_0 \sum_\beta \left[q_0 + (1-q_0)\delta^{\alpha\beta}\right] \left|1 - \frac{\tau^\beta_{sr}(t)}{s_s}\right|^r \tag{23}$$

The function, $g(s_s, h_0)$ represents the sum of squares of the residual d^α:

$$g(s_s, h_0) = \sum_\alpha (d^\alpha)^2 \tag{24}$$

The minimum value of the residual is obtained by calculating the partial derivative of function, $g(s_s, h_0)$

$$f_1(s_s,h_0)=\frac{\partial g(s_s,h_0)}{\partial s_s}=0;f_2(s_s,h_0)=\frac{\partial g(s_s,h_0)}{\partial h_0}=0 \tag{25}$$

By minimizing the residuals, two coupled nonlinear differential equations, (h_0, s_s), are obtained. The initial conjecture value is given and solved by the standard Newton-Raphson program of nonlinear equations, and the final converged values of the hardening parameters, (h_0, s_s), at each time step are obtained. The slip resistance, $\tau_{sr}(t)$, evolves with the deformation in the DDD simulations. The evolution of hardening parameters, (h_0, s_s), with time can be obtained by repeating the above process for each time step of the DDD simulations.

The initial slip resistance,s_0 of the CPFE model influences the initial yielding from the stress-strain curve. In general, the initial slip resistance can be determined through dividing the measured macroscopic yielding stress by the Taylor's factor (Zeng et al., 2016). Therefore, the initial slip resistance is readily estimated from the results of the DDD simulations, including different single crystal orientations. Specifically, the critical resolved shear stress (CRSS) is extracted from the stress-strain curves of the DDD simulations. Here, three values are extracted from the curve, which include the initial yielding stress, 0.02% offset yielding, and 0.04% offset yielding. These yielding stresses are averaged and divided by the Taylor's factor (The details are described in the next section).

The motion of a single dislocation is simulated by MD simulations to obtain the mechanical characteristic parameter (drag coefficient, B), and this parameter is imported into the DDD simulations to model the plasticity and hardening induced by the multiple dislocations. Then, the DDD simulations are coupled with the CPFE model to calculate the hardening parameters, and the massive dislocation collective hardening behavior at the grain level is predicted using the CPFE simulations.

3. Simulation setup and parameter transition

The essence of the multiscale modeling is to predict the mechanical behavior of materials on the basis of physics. Because it needs the huge of time and length scale of the model from the electronic structure to macroscale stress-strain response, it is necessary to model and analyze some key points of the multiscale model. In this case, DDD simulation is used as a bridge between the single dislocation behavior in the nanoscale and mesoscale continuum crystal plasticity model, to calculate the interaction behavior of a large number of dislocations. DDD simulation outputs the decomposition information of each slip system, and then uses the framework in Section 2 to provide the hardening parameters for the CPFE. Since the DDD simulations fluctuate over the time, the hardening parameters of the CPFE are calibrated by smoothing the data fluctuations so that the average values of the parameters are constant after a certain time. By verifying that these values are almost similar after the selected time point, it is reasonable to average the data within the selected time period. This averaging method smears out the interactions between various type dislocations, which is similar to coarse-graining over DDD results containing the giant dislocation groups.

In this work, the strain rates from different scales vary greatly, leading to the difference of time steps in the nano-micron-meso scales. The strain rate of MD simulation is about 10^9 s^{-1}, and the time step is 10^{-10} s; the corresponding values of DDD simulation are 10^4 s^{-1} and 10^{-10} s; and that of CPFE simulation are 10^{-3} s^{-1} and 10^{-2} s. The key to the coupling of the nano-micron-meso scales in the hierarchical multiscale modeling strategy is the parameter transfer between the nano-micron-meso-scale model. In this process, the simulation models at each scale are discussed in detail to test the reliability of parameters at the single and integrated levels.

The atomic scale modeling focuses on the mechanism of the single dislocation behavior (dislocation mobility) as input to the DDD simulations. This method is used in the previous studies, where MD simulations are calibrated the dislocation mobility at the strain rate of 10^9 s^{-1} and used as input for higher scale DDD simulations at the strain rate of $10^2 \sim 10^4$ s^{-1} (Chandra et al., 2015; Li et al., 2022). Because of the large difference of time scales for the DDD and CPFE simulations, the strain rate effect occurs considering these time scales, but this is to make a compromise between the accuracy of prediction results at higher length scales and the computational burden (Chandra et al., 2018). These problems can be solved using the concurrent multiscale models (Chakraborty et al., 2021). However, the parallel multiscale model has the problem of coupled boundary conditions, there is no parallel multiscale model including MD, DDD and CPFE at present (Chakraborty et al., 2021).

In this section, the simulation settings used for the hierarchical multiscale method are presented. The parameters required for the scale transmission under different time- and length- scales are calculated. The MD simulations are applied to obtain the drag coefficient, B, and the dislocation-linear mobility ($V = F/B$) for the DDD simulations. For the single-crystal hardening parameters s_0, $h_0$and s_s with different crystal orientations, we calibrate them with the microscale DDD simulations. For the parameters of the polycrystalline CPFE, the average values of the single crystal parameters for different crystal orientations are used.

3.1. MD simulations

The dislocation mobility required in DDD simulations is obtained by MD simulation. The phonon drag or damping is the main damping, which is controlling the edge dislocations. For the nanoscale MD simulations, this damping is quantified by a drag coefficient, which is an inherent characteristic of the materials and independent of the boundary conditions and strain rates. Some MD simulations reveal that the dislocation type is mainly edge dislocation in the FCC alloy (Olmsted et al., 2005). In addition, the difference of the mobility between the screw and edge dislocations has no obvious effect on the strain-hardening behavior in DDD simulations (Cai et al., 2004; Groh et al., 2009; Zhou et al., 2010). Thus, in the current work, the MD simulations only focus on the edge dislocations.

To compute the dislocation mobility in the Al0.1FeCoCrNi MPEA, the dislocation line is inserted in the simulation cell based on the Burgers vector. The MD simulations are performed using an open source LAMMPS code (Plimpton, 1995) and visualized using an Ovito package (Stukowski, 2009). The inter-atomic potential employs the embedded atom method (EAM) potential (Farkas and Caro, 2020), which is in good agreement with various properties of the Al0.1FeCoCrNi MPEA, including the dislocation behavior under the deformation. The sizes of the sample with about 393,300 atoms are 30.0 × 14.0 × 10.0 nm^3. It has been confirmed that the size of the cell has no effect on the calculated drag coefficient.

A ½[1$\bar{1}$0] edge dislocation is inserted at the center of the simulation box, where its line direction is $y = [11\bar{2}]$, the slip direction is $x = [1\bar{1}0]$, and the normal of the glide-plane is $z = [111]$. Burgers vector is $b = 2.52 \times 10^{-10}$ m. The periodic boundary conditions are along the x and z directions, and the fixed boundary condition is along the y direction (Fig. 2). The sample is initially relaxed and equilibrated at the targeted temperature with the pressures in the x- and z- directions equilibrated to zero through the isothermal-isobaric (NPT) ensemble for 100 ps. Then, the system is relaxed under the canonical (NVT) ensemble for 100 ps. The motion of the dislocation at every time step is monitored. With the increase of a shear load, an a/2[1$\bar{1}$0] edge dislocation experiences a significant local motion and continuous slip under the loading.

Fig. 3 shows the evolution of the velocity of an edge dislocation in the Al$_{0.1}$FeCoCrNi MPEA with the ratio of different shear stresses to temperature by MD simulations. In the range of the applied stress that we tested, the dislocation velocity increases almost linearly with σ/T, which is in-line with the phonon damping theory (Brailsford, 1972; Olmsted et al., 2005):

$$v = v_0 + (b\sigma / T)\Gamma, \quad \Gamma = B/T \tag{26}$$

where σ is the ratio of the shear stress to temperature, and B is the drag coefficient. Based on the linear mobility law, the drag coefficient is $B = 2.20602 \times 10^{-4}$ Pa·s at 300 K. The dislocation mobility predicted by MD simulations can be used as an input for the microscale DDD simulations to quantitatively predict the collective behavior of a great quantity of dislocations in the Al$_{0.1}$FeCoCrNi MPEA, and then the hardening parameters are obtained for the CPFE simulations.

3.2. DDD simulations

All DDD simulations in the current work are performed by a ParaDiS program (Bulatov et al., 2006). The dislocation hardening behavior of the FCC Al$_{0.1}$FeCoCrNi MPEA is obtained using DDD simulations. The material parameters of the Al$_{0.1}$FeCoCrNi MPEA are listed in Table 1. At present, the DDD package is only available for simulations based on the isotropic assumption. However, the results so obtained are generally accepted by the materials community (Rao et al., 2019; Zhang et al., 2021; Wei et al., 2019; Chandra et al., 2018). Therefore, the same shear modulus is used for the DDD simulations with different tensile orientations. Based on the previous DDD simulations (Lehtinen et al., 2018; Arsenlis et al., 2012), the cube simulation box is set up with the periodic-boundary conditions and a size of 2 μm. The initial dislocation density is $\rho_0 \approx 5.5 \times 10^{12}$ m^{-2}, which is consistent with the previous result measured experimentally (2 × 10^{12} m^{-2} to 5 × 10^{13} m^{-2}) (Dimiduk et al., 2005; Norfleet et al., 2008). Then, these dislocations are evenly distributed on 12 slip systems, and relaxed without a load. The strain rate is $\dot{\varepsilon} = 10^4$ s^{-1} (Fan et al., 2021), and the crystallographic orientations are along [001], [112], [111], [212], [101], [102], and [213].

Since the phase structure is stable over a wide temperature range in the FCC MPEA with a low Al content, the precipitation is difficult to generate. Therefore, the lattice distortion effect in the Al$_{0.1}$FeCoCrNi MPEA is mainly considered in the current model (Gangireddy et al., 2019). In order to capture the effect of a heterogeneous lattice strain field induced by the lattice distortion on the strain hardening in the MPEAs, a 3D lattice-strain field needs to be developed and embedded into DDD simulations. Based on the experimentally-measured lattice-strain field of the Al$_{0.1}$FeCoCrNi MPEA, the fractal characteristics of the lattice-strain field are confirmed. Therefore, we use the generalized Weierstrass-Mandelbrot (W-M) fractal function to construct the 3D lattice-strain field fractal function (Ausloos and Berman 1985; Yan and Komvopoulos 1998):

$$\varepsilon\left(\mathbf{r}\right) = \mathrm{H}^{\mathrm{D}-3}\left(\frac{\ln\gamma}{M}\right)^{\frac{1}{2}} \sum_{m=1}^{M} \sum_{n=0}^{n_{\max}} \left[\cos\left(\phi_{m,n}\right) - \cos\left(\frac{2\pi\gamma^n \vec{n}_m \cdot \mathbf{r}}{L} + \phi_{m,n}\right)\right]\left(\frac{\gamma^n}{L}\right)^{\mathrm{D}-4} \tag{27}$$

where $\mathrm{k}_0 = \frac{2\pi}{\mathrm{L}}$ is a wavenumber, $n_{\max} = \mathrm{int}\left[\frac{\log(L/L_s)}{\log\gamma}\right]$ is the upper limit, and $L_s = 4\mathrm{b}$ is the cut-off size. γ =1.5 is the frequency density, M =50 is the number of superposed ridges, $\vec{n}_m$ is unit vectors evenly distributed in a unit 3D hypersphere, and $\phi_{m,n}$ is a random phase. D

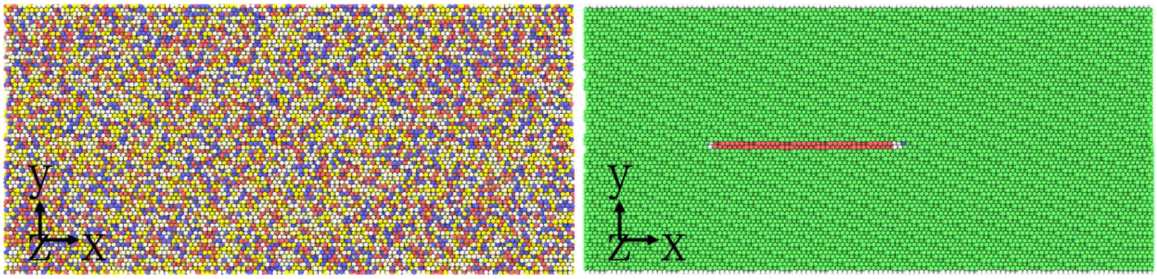

Fig. 2. MD simulation cell of dislocation mobility for the edge dislocation gliding on the (111) plane.

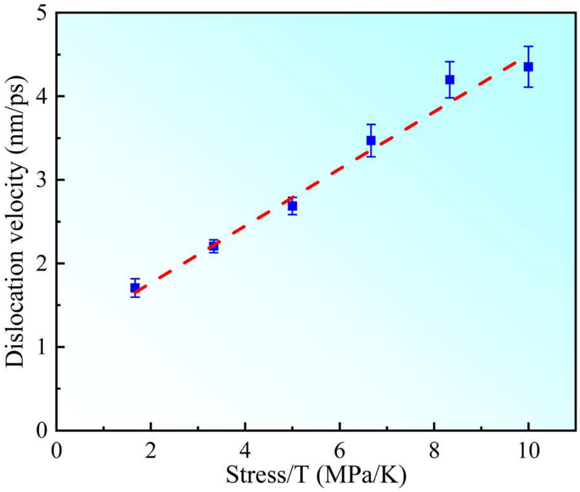

Fig. 3. Relationship between the edge-dislocation velocity and applied shear stress divided by temperature (σ/B) in a single crystal $Al_{0.1}$FeCoCrNi MPEA.

Table 1
Material parameters in DDD simulations for the $Al_{0.1}$FeCoCrNi MPEA.

Parameter	Symbol	Value
Shear modulus	μ	80.1 GPa
Poisson's ratio	v	0.3
Magnitude of Burgers vector	*b*	0.252 nm
Dislocation radius	r_0	5*b* nm

and H are the fractal dimension and strain amplitude (Table 2), which are obtained using the structure-function method (Wu, 2002) and the lattice strain field of the $Al_{0.1}$FeCoCrNi MPEA measured experimentally (Shao et al., 2019). According to the experimentally measured lattice strain field of the $Al_{0.1}$FeCoCrNi MPEA (Shao et al., 2019), L = 200 nm is equal to the sample size.

The stress field, $\sigma^{mpea}(s)$, from the lattice strain is obtained by the generalized Hooke's law:

$$\sigma_{\mathrm{ij}} = 2G\varepsilon_{ij} + \lambda\varepsilon_{kk}\delta_{ij} \tag{28}$$

To eliminate the non-equilibrium caused by the random phase, the 3D strain-field function should minus the average value, $\bar{\varepsilon}$, of the entire DDD simulation. This box is obtained from 100 × 100 × 100 evenly distributed discrete points, $\bar{\varepsilon} = \sum_k\sum_m\sum_n \varepsilon(x_{\mathrm{k}}, y_m, z_n, \mathrm{H}, \mathrm{D}, \varphi_{\mathrm{m,n}})$ $/10^6$ (k, m, $n = 1\ldots100$).

The effect of mobility of the edge and screw segments on the stress-strain curve of the $Al_{0.1}$FeCoCrNi single crystal along [001] orientation has been investigated by DDD simulations. Fig. 4 shows that the stress-strain curves for various dislocation mobility do not vary significantly in comparison to the curve for the same mobility. Consequently, different mobility values used in the DDD simulation do not bring an appreciable change in the prediction of the calibrated hardening parameters (Chandra et al., 2018). In addition, the existing MD simulations indicate that the difference of the drag coefficients between the edge dislocation and screw dislocation is small in the FCC FeNiCrCoCu HEA (Shen and Spearot, 2021). Therefore, as with other DDD simulation studies of the FCC crystals, only the mobility of the edge dislocation is considered (Sills et al., 2018; Lu et al., 2019; Rao et al., 2019).

In Section 2, the total plastic-strain rate for all slip systems is set as the constant value in the MPEAs, which is certificated by investigating the relationship between the total plastic-shear strain for all slip systems of the $Al_{0.1}$FeCoCrNi MPEA. The evolution of the total plastic-shear strain shows that the plastic-shear strain increases linearly with time in the $Al_{0.1}$FeCoCrNi MPEA along the [212] direction (Fig. 5). The slope is applied to characterize the plastic-shear strain rate. It is worth noting that the total plastic-shear strain

Table 2
The fractal dimension and strain amplitude for the strain components in the $Al_{0.1}$FeCoCrNi MPEA according to the experimental data (Shao et al., 2019).

Strain components	ε_{xx}	ε_{yy}	ε_{zz}	ε_{xy}	ε_{xz}	ε_{yz}
Fractal dimension, D_{ij}	D_{xx}	D_{yy}	D_{zz}	D_{xy}	D_{xz}	D_{yz}
	3.9065	3.8855	3.8961	3.9281	3.9281	3.9281
Strain amplitude, H_{ij} ($\times 10^{-4}$)	H_{xx}	H_{yy}	H_{zz}	H_{xy}	H_{xz}	H_{yz}
	5.539	5.539	5.539	3.2659	3.2659	3.2659

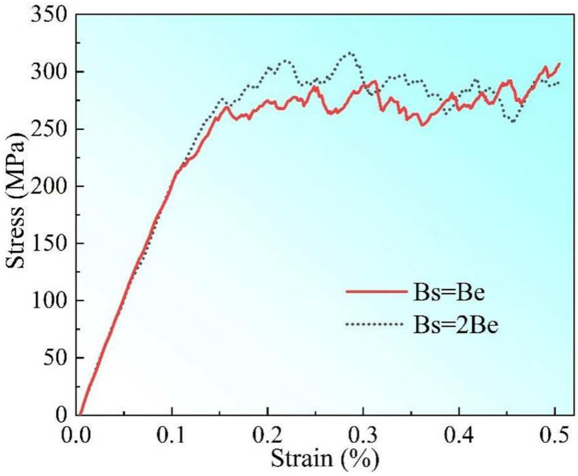

Fig. 4. Comparison of stress-strain curve for the FeCoCrNiAl0.1 single crystal along [001] orientation obtained from DDD simulations at various dislocation mobility.

rate from the slope in Fig. 5 ($9.84 \times 10^3\ \mathrm{s}^{-1}$) is close to the load strain rate ($1 \times 10^4\ \mathrm{s}^{-1}$). Therefore, the total plastic-slip rate is obtained by the relationship between the total plastic-shear strain and time, which is in equilibrium with the applied strain rate using the DDD simulations during the plastic deformation.

Fig. 6 shows the relationship between the stress and strain in the FCC $\mathrm{Al}_{0.1}$FeCoCrNi MPEA along [001], [112], [111], [212], [101], [102], and [213] crystal orientations from DDD simulations. The yielding stress difference for various load directions is caused by the Schmid factor, which dominates the active dislocation-slip systems. In the plastic deformation stage, the serration occurs in the stress-strain curve for all the considered crystal orientations (Fig. 6), which is caused by the initial dislocation density being incapable of coping with the strain rate during the deformation.

The initial slip resistance,s_0, in the CPFE model for different single crystal orientations, is estimated from the initial yielding of the stress-strain curve. Specifically, the CRSS is extracted from the stress-strain curves from the DDD simulations. Due to the obvious fluctuation of the curve (Fig. 6), the extract values for each crystal orientation show the first deviation form linearity, 0.02% offset yielding, and 0.04% offset yielding. Then, we average these yielding stresses, and multiply them by Schmidt factors, respective. The initial resolved slip resistance of the CPFE model is listed in Table 3 for a single-crystal $\mathrm{Al}_{0.1}$FeCrCoNi MPEA with different loading orientations.

The DDD simulations output the resolved stresses of all active slip systems, and then provide hardening parameters for the CPFE model. The forest hardening is widely used to investigate strain hardening in alloys (Devincre et al., 2006; Zhou et al., 2010; Shehadeh, 2012). The dislocation hardening meets the Taylor law as:

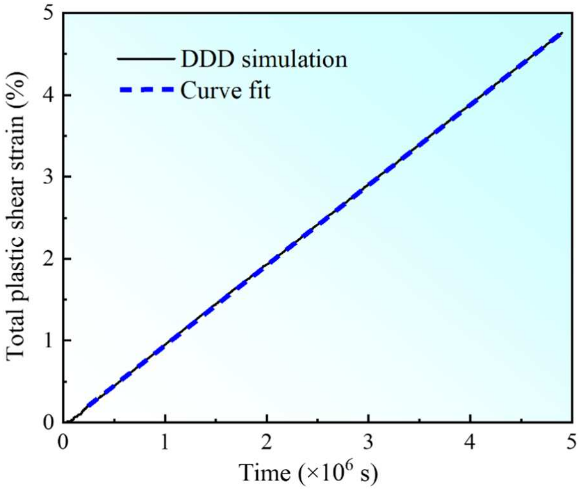

Fig. 5. The relationship between the total plastic-shear strain over all slip systems and time in DDD simulations in the FCC $\mathrm{Al}_{0.1}$FeCoCrNi MPEA along the [212] orientation.

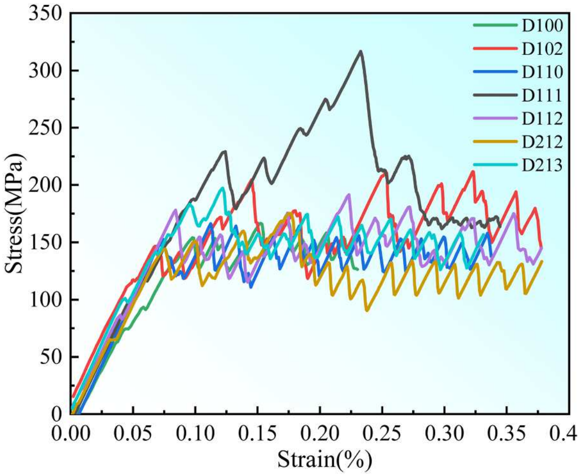

Fig. 6. The mechanical responses of the single crystal $Al_{0.1}FeCrCoNi$ MPEA at different loading crystal orientations using DDD simulations.

Table 3
Hardening parameters from DDD simulations for different load directions of the single crystal $Al_{0.1}FeCoCrNi$ MPEA.

Orientation	[001]	[102]	[101]	[111]	[112]	[212]	[213]
s_0 (MPa)	60.37	71.56	59.34	57.53	62.02	55.65	80.05
h_0 (MPa)	359.74	303.87	304.08	402.34	343.45	312.51	285.05
s_s (MPa)	492.46	405.82	396.49	581.75	509.05	407.84	388.58

$$\tau = \alpha \mu b \sqrt{\rho} \tag{29}$$

where μ is the shear modulus, b is the magnitude of the Burgers vector, ρ is the dislocation density, and α is the dislocation hardening parameter. The evolution of dislocation hardening parameter with the increased strain is obtained by the Taylor law. In the traditional alloys, the dislocation hardening parameter in the forest hardening ranges from 0.25 to 0.45 for the dislocation density about 10^{12} m^{-2} (Madec, 2001). The lattice distortion hinders the dislocation movement, and the resolved shear stress in the MPEAs is higher than that in the traditional alloys for the same dislocation structure. Therefore, α is higher in MPEAs than that in traditional alloys using DDD simulations (Fig. 7). From the change trend of the stress-strain curve, the data computed by the DDD simulations is intermittent. Therefore, in order to obtain the average value of the hardening parameter for the CPFE model, the DDD simulations need the time averaging. Fig. 7 shows the evolution of dislocation hardening parameter with the increasing time for the $Al_{0.1}FeCrCoNi$ MPEA along the [212] crystal orientation, in which there are two different regions (separate with a black solid line). The value of α is seriously jumping in the first region because the initial dislocation structure cannot match the deformation rate of loading. As the strain

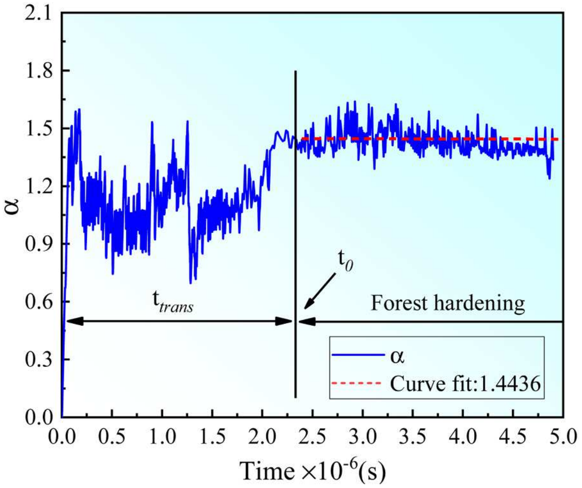

Fig. 7. The evolution of the dislocation hardening parameter as a function of time along the [212] crystal orientation.

increases, the dislocations begin to move and proliferate. Subsequently, the dislocation hardening parameter in the second regime fluctuates slightly around a constant value of 1.44 (a red dashed line, as shown in Fig. 7), indicating that the current dislocation structure (after the multiplication and movement of dislocations) matches the deformation rate to reach the strain hardening stage.

Based on the above the smooth region of the dislocation hardening parameter evolution and the theoretical framework of hierarchical multiscale in Section 2.4, the hardening parameters, h_0 and s_s, with the increasing time are presented in Fig. 8. The fluctuations of hardening parameters tend to be a constant value (Fig. 8). The average values of hardening parameters for time, $t > t_0$, are distill (a blue solid line and red dotted line parallel to the *x*-axis), and applied to the crystal plasticity models to capture the mechanical response of the $Al_{0.1}$FeCrCoNi MPEA at the microscale. The average fluctuations of the hardening parameters do not obviously change with the increasing time. The hardening parameters of the single crystal $Al_{0.1}$FeCrCoNi MPEA with different loading orientations are listed in Table 3.

3.3. CPFE simulation

The quasi-static deformation of the single crystal and polycrystalline $Al_{0.1}$FeCoCrNi MPEAs under the uniaxial tension is presented using the CPFE simulations, to explore the deformation behavior at the mesoscale. The effectiveness of the current method is verified by the comparison of the experimental result and CPFE result (Jiang et al., 2020). The CPFE simulations are performed using an open-source PRISMS-Plasticity framework (Yaghoobi et al., 2019), and a finite element method (FEM) code is built on top of the deal.II open-source FEM library (Bangerth et al., 2007). The results are visualized using an open-source software package Paraview (Ahrens et al., 2005). The material flow-rule parameters (Eq. (15)) used in the crystal plastic model are estimated from the previous literature, as listed in Table 4. The anisotropic elastic constants of the $Al_{0.1}$FeCoCrNi MPEA (C_{11}, C_{12}, and C_{44}) are calculated by the MD simulations and confirmed by the references (Gnäupel-Herold et al., 1998; Jiang et al., 2020). The hardening parameters (s_0,s_s, and h_0) are calculated using the DDD simulations.

3.4. Single crystals

A finite element model with a box size of 1000 μm × 1000 μm × 2000 μm is established using 3D-brick elements, to simulate the mechanical response of a single crystal $Al_{0.1}$FeCoCrNi MPEA under the uniaxial tension (Fig. 9a). The model is discrete by 16,000 (20 × 20 × 40) C3D8 (one integration point) hexahedral finite elements. The z-axis of the reference frame is oriented along the crystal directions of [001], [102], [101], [111], [112], [212], and [213]. Then the specimen is uniaxially stretched along the z-axis at room temperature with a constant strain rate of 10^{-3} s^{-1}. The tensile loading is applied employing a variable positive displacement at the top of the simulation box, keeping a zero displacement for the bottom of the simulation box along the z-axis, and setting two nodes fixed at the bottom of the simulation box to avoid the rigid-body movement. The final solution is obtained in 2000 time increments with an initial time step of Δt=0.1 s. The maximum number of the nonlinear equilibrium iterations is 4 for each increment.

In order to capture the mechanical response of the polycrystalline $Al_{0.1}$FeCoCrNi MPEA, we select 7 single crystal directions at the edge and center of the stereographic triangle, as shown in Fig. 9(b). The crystal plasticity calculations are carried out for 7 crystal orientations of the single-crystal $Al_{0.1}$FeCoCrNi MPEA, to predict the stress-strain response.

Table 4 shows the elastic-parameter values (C_{11}, C_{12}, and C_{44}) and the constitutive parameters of the CPFE model Eqs. (15)–((17)), to simulate the mechanical response of the $Al_{0.1}$FeCoCrNi MPEA. The constitutive parameters ($\dot{\gamma}_0$, r, h_0, s_0, and s_s) are assumed to be the same and fixed for all 12 slip systems. These values serve as the input parameters of the CPFE simulations (Sundararaghavan et al., 2008; Lu et al., 2020). The hardening parameters are calculated using DDD simulations for different single crystalline orientations in

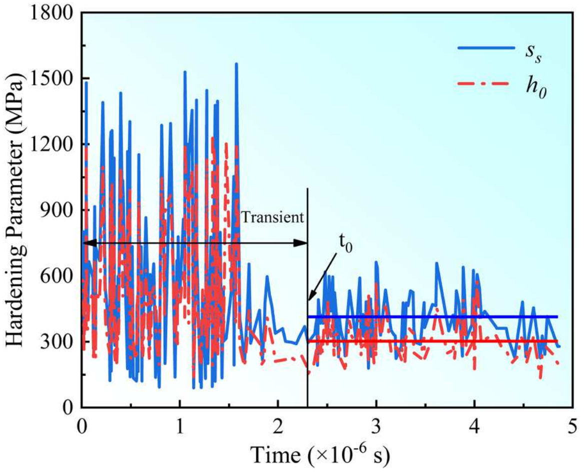

Fig. 8. The evolution of hardening parameters, s_s, and, h_0, with the time in the single crystal $Al_{0.1}$FeCrCoNi MPEA along the [212] orientation using DDD simulations. The horizontal line represents an average value of the hardening parameters extracted over a period of time ($t > t_0$).

Table 4
Material parameters used to simulate the mechanical responses of the single crystalline and polycrystalline $Al_{0.1}$FeCoCrNi MPEAs.

Symbol	Description	Value
C_{11}	Elastic constants	275.31 GPa (Jiang et al., 2020)
C_{12}	Elastic constants	107.02 GPa (Jiang et al., 2020)
C_{44}	Elastic constants	106.59 GPa (Gnäupel-Herold et al., 1998; Jiang et al., 2020)
m	Strain-rate-sensitivity exponent	0.04
$\dot{\gamma}_0$	Reference shearing rate	10^{-3} s^{-1} (Kalidindi, 1992)
q_0	Latent-hardening parameter	1.4 (Anand et al., 1996)
r	Hardening exponent	2.25 (Anand et al., 1996)
s_0	Initial slip resistance	From DDD simulations
h_0	Initial hardening modulus	From DDD simulations
s_s	Saturation stress	From DDD simulations

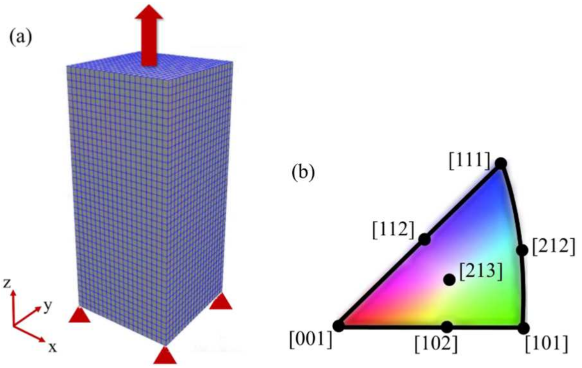

Fig. 9. The tension model of a single crystalline CPFE simulation (a). The specific crystal orientation at the edge and center of the stereographic triangle (b).

the previous section. The parameter of a single crystal is used to quantify and calibrate the hardening parameters of a polycrystal.

3.5. Polycrystalline

The finite element model geometry is generated in the open-source software package of DREAM.3D (Groeber et al., 2014), and meshed using the modules of the open-source software PRISMS-Plasticity (Yaghoobi et al., 2019). Compared with the Voronoi tessellation, the grains from the polycrystalline RVE generated in DREAM.3D is much more realistic (Knezevic et al., 2014). Fig. 10(b) shows that the RVE contains 200 grains and discrete by 32 × 32 × 32 C3D8 finite elements. As well known, compared with traditional alloys, the microstructure characteristics of grain boundaries in the MPEAs are more complex due to their severe lattice distortions. In addition, although some crystal plasticity models considering the influence of grain boundary have been developed, there is no highly recognized model and no model has been widely used (Lu et al., 2020; Ganesan et al., 2021; Lakshmanan et al., 2022). Therefore, the effect of grain boundary does not be considered in the current crystal plastic model. Compared with a tetrahedral mesh, the hexahedral mesh can post-process the results faster and visualize them easier. We have tested the amount of grains and elements sufficient to

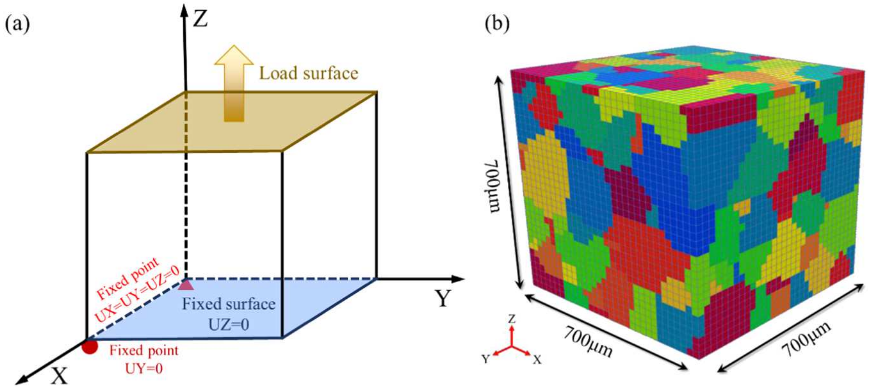

Fig. 10. The boundary condition for the polycrystal (a). The model diagram of RVE including 200 random distribution grains (b).

accurately capture the mechanical response of a polycrystalline $Al_{0.1}$FeCoCrNi MPEA (in the next section). This trend would not lead to stepped-like grain boundaries, which makes the predicted stress-field inhomogeneity. Since there is no significant texture in the EBSD measurement (Gangireddy et al., 2018), the random grain orientations represent an approximately isotropic block. Fig. 11 shows the pole figures in the polycrystalline MPEAs.

The boundary and loading conditions applied to RVE are presented in Fig. 10(a). For the simplicity, the degrees of freedom along the axes of *X, Y*, and *Z* are represented as *UX, UY* and *UZ*, respectively. To prevent a rigid body displacement during the loading, $UZ = 0$ is set at the bottom of RVE, $UX = UY = UZ = 0$ on the point at the coordinate origin, and $UY = 0$ at the outermost point of the X axis. The top of RVE is the loading surface with the variable positive displacements and quasi-static strain rates, to simulate the uniaxial tension at room temperature (Stopka et al., 2021).

4. Result and discussion

In this section, the results of the mesoscale CPFE simulations in the $Al_{0.1}$FeCoCrNi MPEA are presented. The hardening parameters of different single crystal orientations are calculated using the DDD simulations, and the hardening parameters of the polycrystalline system are obtained by calibrating the single crystal hardening parameters.

4.1. Single crystal

The mechanical responses of a single crystal with different crystal orientations are predicted by CPFE simulations, as exhibited in Fig. 12. Compared with the [001]-[111] symmetry axis, the strain hardening rates in the stress-strain curves of other orientations, such as [212] and [213], are closer to the [101] zone axis in the standard stereographic triangle. Except for [111], the yielding strengths of other crystal orientations range from 100 to 150 MPa. The hardening parameters (Table 3) calibrated by DDD simulations also reflect the work hardening rates. The results show that the hardening parameters along the [111] orientation are the highest, which are 402.3 MPa, and 581.7 MPa. These work hardening behaviors of the single crystals have been widely discussed in the past (Moon et al., 2018; Kireeva et al., 2020; Kawamura et al., 2021). Since our main objective is the successful implementation of a hierarchical-multiscale theory, these aspects would not be discussed.

Table 5 shows the Schmidt factors of the corresponding crystal orientations in the $Al_{0.1}$FeCoCrNi MPEA. The Schmidt factor of [111] is equal to 0.27, which is quite different from other orientations, and the corresponding hardening behavior is stronger. The maximum Schmidt factor is 0.49 for [101] and [102]. Accordingly, their stress-strain slopes are flat, as shown in Fig. 12. The difference of hardening behaviors in distinct crystal orientations is due to different Schmidt factors in crystal orientations, and the shear stress required for the dislocation activation is distinct. Therefore, different dislocation proliferation rates lead to the difference of strain-hardening rates (slopes of a stress-strain curve) between different crystal orientations.

4.2. Polycrystals

It is very difficult and time-consuming to carry out authoritative experiments on the mechanical behavior of the single crystals in multiple orientations. Concurrently, it is difficult to model the mechanical behavior of the polycrystalline RVE at present. Therefore, the deformation characteristics of the polycrystalline materials is quantified by fitting the mechanical response of the polycrystalline RVE with the corresponding experimental curve (Li Y et al., 2013; Prithivirajan et al., 2018; Baudoin et al., 2019; Bandyopadhyay et al., 2020; Lu et al., 2021).

In the process of the deformation of the polycrystalline materials under the uniaxial loading, the boundary conditions of grains are more complex than a single-crystal uniaxial loading experiment due to the interaction of the surrounding grains. Hence, it is rather cumbersome to accurately represent the mechanical responses of polycrystals aggregates containing such the complex boundary conditions. Previously, the plastic response of the polycrystal is usually quantified, using the average single crystal response of the appropriate Taylor factor in the [100] and [111] orientations. However, the predicted polycrystalline material has obvious deviation from the experimental response curve under the large deformation. More recently, the hardening parameters of a polycrystalline RVE are calibrated using the average values of hardening parameters in seven directions of the single crystals (Chandra et al., 2018),

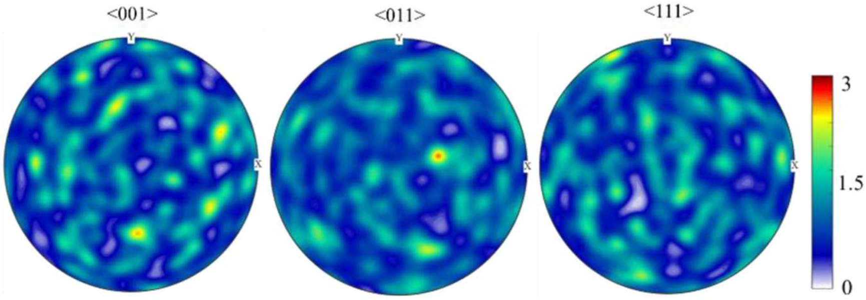

Fig. 11. The representation of an initial texture of the $Al_{0.1}$FeCoCrNi MPEA simulated by a set of 200 grains.

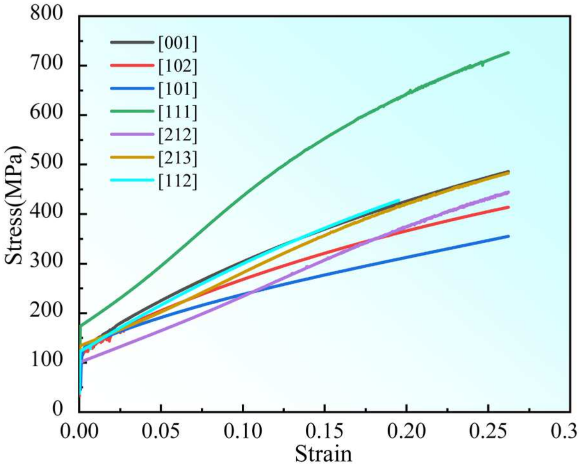

Fig. 12. The strain-stress curves for the seven groups of crystal orientations.

Table 5
The Schmid factors of the $Al_{0.1}$FeCoCrNi MPEA under different loading directions.

Dislocation slip system	Loading direction [001]	[102]	[101]	[111]	[112]	[212]	[213]
Schmid factor	0.41	0.49	0.49	0.27	0.41	0.41	0.47

revealing the deformation mechanisms of Cu. Although the deformation curve is consistent with the experiment, the initial slip resistance still needs to fit the experimental curve. Because the boundary conditions of the RVE grains are more complex than that in a single crystal, CRSS in the polycrystal can not be characterized by a simple average of the single crystal. Our previous work (Li et al., 2020) has accurately predicted the CRSS of MPEAs (including FCC and BCC alloys). Therefore, the CRSS can be easily calculated in the $Al_{0.1}$FeCoCrNi MPEA, and divide by the Taylor's factor of 3.05 to obtain s_0 (62.5MPa) (Zeng et al., 2016). Other hardening parameters, h_0 and s_s, for seven single crystal orientations have been quantified in the hierarchical multiscale modeling in the previous sections, as shown in Table 2. The relationship between different orientations is to establish, for obtaining the single crystal and polycrystalline hardening parameters. After several ways, h_0 and s_s present approximately normal distributions. Fig. 13 shows the distribution histogram of hardening parameters. The average values of h_0 and s_s are 330 MPa and 454 MPa, respectively.

Now, the hardening parameters of the polycrystalline $Al_{0.1}$FeCoCrNi MPEA would be obtained. In order to improve the efficiency of simulation and fully capture the mechanical response of the polycrystalline MPEAs, the effects of the elemental number and grain number on the simulation results should be investigated. The stress-strain response curves of RVEs with the same number of grains (i.e., 200) and different numbers of finite elements are plotted in Fig. 15(a). The results show the mechanical responses of RVEs

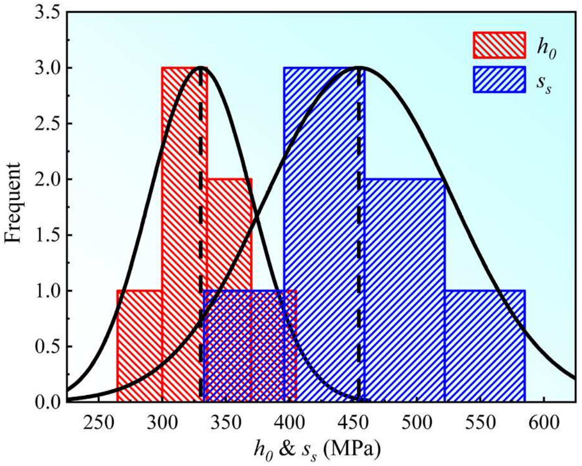

Fig. 13. Distribution histogram of the single crystal hardening parameters (h_0 and s_s), where the dotted line is the average value of hardening parameters.

containing 32,768 (32 × 32 × 32) elements almost converge. The RVEs with different numbers of grains are established, and their grain orientations are random as previously described (Fig. 14(a)). Four RVEs during the uniaxial tension are simulated, and all other conditions are the same. As shown in Fig. 14(b), the stress-strain curves approach gradually the same value with the increasing grain number. From 200 to 400 grains, the stress-strain curves are nearly overlapped. Therefore, for obtaining a balance of the calculated accuracy and cost, 32,768 (32 × 32 × 32) elements and 200 grains are used to represent the polycrystalline model.

Fig. 15(b) shows that the mechanical response of the $Al_{0.1}FeCoCrNi$ MPEA polycrystalline RVE at strain rates of $1 \times 10^{-3}\ s^{-1}$ and $2.5 \times 10^{3}\ s^{-1}$. The experimental data (Wu et al., 2017; Jiang et al., 2020) is added for the comparison. The results show that the simulated stress-strain curve at a quasi-static strain rate of $1 \times 10^{-3}\ s^{-1}$ is in good agreement with the experimental data. The variation of the maximum stress is within 26 MPa, which verifies our calibration procedure. Fig. 16 shows the microstructural deformation of RVE at 1%, 5%, 10% and 20% strain stage. The simulated stress-strain curve with a strain rate of $2.5 \times 10^{3}\ s^{-1}$ is obtained by changing the strain rate of $1 \times 10^{-3}\ s^{-1}$, and keeping all other conditions, including hardening parameters and flow parameters of simulation constants. It can accurately predict the mechanical response of the $Al_{0.1}FeCoCrNi$ MPEA at $2.5 \times 10^{3}\ s^{-1}$ strain rate within 8%.

The detection of the local microscale strain plays a significant role for the optimization of the microstructures, which would enhance obviously the mechanical property. Fig. 17 shows the position and grain shape of the RVE section. The strain distribution is investigated at the applied strains of 0.05%, 0.1%, 0.5%, and 1%, as presented in Fig. 18, in order to study its effect on the plastic deformation. Considering the crystal orientation hardening behavior, the grain orientation leads to the softening from some grains, which appear to be sensitive to the anisotropic strain responses even if the same loading conditions. Namely, the adjacent grains have the extremely contrasting strain distributions. Subsequently, when the sample enters the yielding stage, the strain amplitude increases and the deformation region basically maintains the original state (Fig. 18b, f). In the strain hardening stage, the strain amplitude is further increased, and a few overly high strain regions even appear in the original low strain region. Especially, there is no obvious consistent relationship between the strain and stress, suggesting that the high strain region corresponds to the low stress region (Fig. 18c, g and d, h). Here, the higher local stresses occur in some low strain regions. In particular, the probability statistics of strain and stress distribution for different strain stages is counted in Fig. 18 i, j. With the increasing tensile deformation, the average values of strain and stress increase (corresponding to the stress-strain curve), the inhomogeneity of the high strain and stress region at the corresponding stage also increases. In other words, this result suggests that a strong stress/ strain gradient exists with the increase of applied loading (Fig. 18 i, j), resulting in an important contribution to the material strength. In the experiment, it is easier to capture the strain field by an *in-situ* observation equipment. Thus, the strengthening mechanism of MPEAs can be revealed by analyzing the distribution law of the strain field. Hence, in addition to the nanoscale dislocation evolution, the heterogeneous strain distribution may be an important reason for the enhanced strength at the micron scale. Fig. 19 shows the pole figures of the extracted grain orientations from the simulated data with the increase of the tension strain. The more newly-added local extreme points indicate that the orientation of some grains would change significantly. This trend may be to adapt to the incongruous deformation behavior in the later stage of work hardening.

4.3. Strain rate

The strain rate plays a great influence on the mechanical properties of the FCC MPEAs (Jiang et al., 2020). In the comparison of the static or quasi-static loading process, the metal materials show some obvious behaviors at the high strain rate loading (Park et al., 2018). In addition, under the dynamic conditions, the dislocation motion is quietly different due to the viscous resistance effect (Meyers, 1994). Therefore, it is necessary to study the mechanical response of the $Al_{0.1}FeCoCrNi$ MPEA at different strain rates. Here, the mechanical responses and stress-strain distributions of the polycrystalline $Al_{0.1}FeCoCrNi$ MPEA are predicted at different applied strain rates of $10^{-2}\ s^{-1}$, $10^{-1}\ s^{-1}$, $1\ s^{-1}$, $10\ s^{-1}$, and $10^{2}\ s^{-1}$. In the current CPFE simulations, the reference strain rate is $10^{-3}\ s^{-1}$. Fig. 20 shows the stress-strain responses of the polycrystalline $Al_{0.1}FeCoCrNi$ MPEA at different strain rates. With the increase of the strain rate, the yielding stress increases monotonically under the same strain, and the slope of the stress-strain curve increases gradually. It is obvious that this result is consistent with the experimental observation (Moon et al., 2018; Kireeva et al., 2020).

Fig. 21 shows that a high strain rate causes the large strain and stress stored in grains. At the same time, higher strain gradients are generated in the adjacent grains with the increased strain rate (Fig. 21a–e). This interesting observation also appears in the stress fields (Fig. 21f–j). In other words, the extremely-high deformation gradients can handle the energy brought by higher strain rates in the MPEAs (Miracle and Senkov, 2017; Pan et al., 2021), revealing the root cause of a good energy absorption capacity. The comparison of the pole figures shows that the high extreme points appear in almost the same position. The trend indicates that the grain rotation hardly occurs (Fig. 22). Thus, the good energy absorption characteristics of the MPEAs depends upon the strong deformation gradient.

Although the current work is trying its best to establish the dislocation-based strengthening and toughening of MPEAs using the multiscale simulations of the close correlation among the nanoscale, micronscale and mesoscale, the other key microstructures, such as the deformation twinning, interstitial element, and precipitate, also play a key role in their mechanical properties. The deformation twinning not only greatly improve the plasticity at low temperatures (Gludovatz et al., 2014), but also enhances the strength of MPEAs at room temperature (Jo et al., 2017; Zhang et al., 2017; Huang et al., 2018). For example, the recent experimental studies (Yu et al., 2016; Choudhuri et al., 2018; Huang et al., 2021) show the deformation twinning take place at a later stage of the plastic deformation process in the Al0.1CuCrFeNi MPEAs due to the low stacking fault energies, resulting in the improvement of the MPEA strength. However, it would be considered in the future for the following two reasons: (i) Lack of a reasonable deformation twin strengthening model for MPEAs due to their unique atomic scale serious lattice distortions, extremely different from the conventional alloys; (ii) Lack of the experimental quantitative data to determine the twin volume fraction and thickness using the synchrotron-based X-ray micro-diffraction experiment. Hence, the present work only focuses on the dislocation-related strengthening and plasticity.

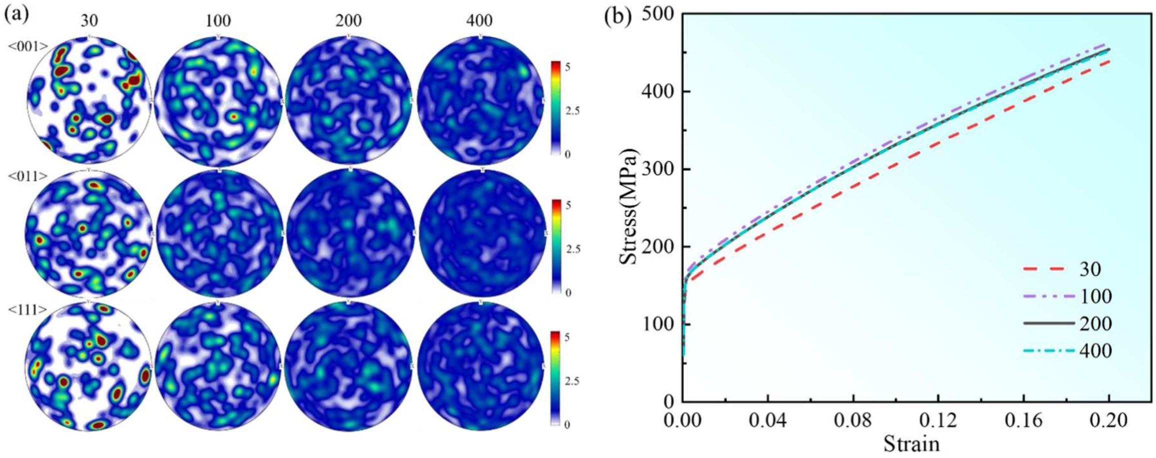

Fig. 14. (a) Representation of an initial texture of the Al0.1FeCoCrNi MPEA simulated at the grain number of 30, 100, 200, and 400. (b) Comparison of RVE mechanical responses with different numbers of grains (elements: $32 \times 32 \times 32$).

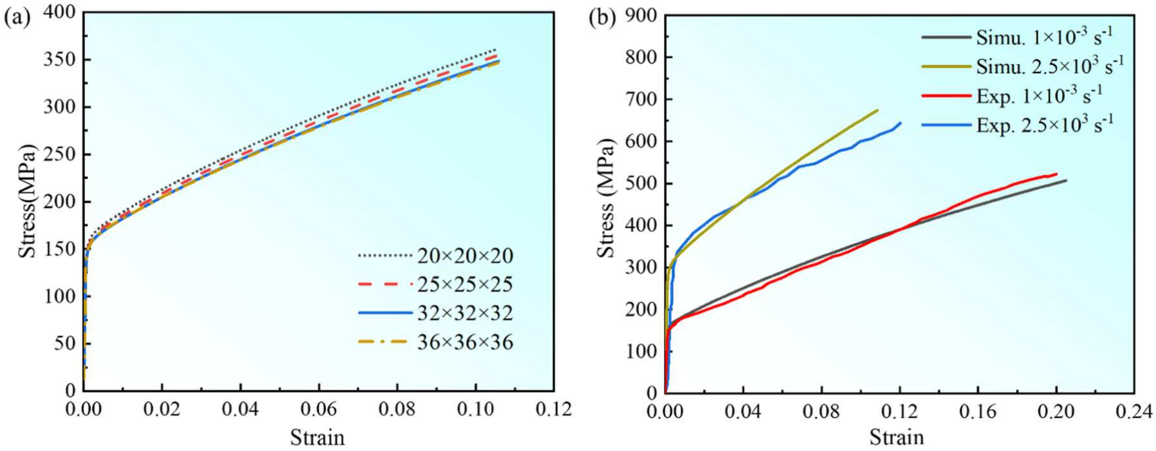

Fig. 15. (a) Comparison of RVE mechanical responses with different numbers of elements (grains: 200). (b) The predicted and experimental stress-strain curves of polycrystals at the strain rates of 1×10^{-3} s^{-1} and 2.5×10^{3} s^{-1}.

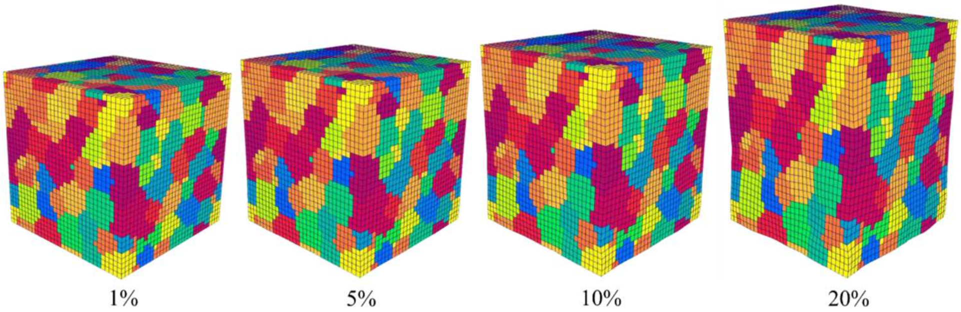

Fig. 16. The comparison of the microstructural deformation of RVE at 1%, 5%, 10% and 20% strain stage.

5. Conclusion

In this study, we propose a multiscale modeling method that can capture the effect of the nano-micron-meso-scale structure on the mechanical properties of the MPEAs. The elastic parameters and dislocation resistance coefficients required for the microscale DDD simulations are extracted from the nanoscale MD simulations, and then the lattice distortion strain field caused by the atomic mismatch

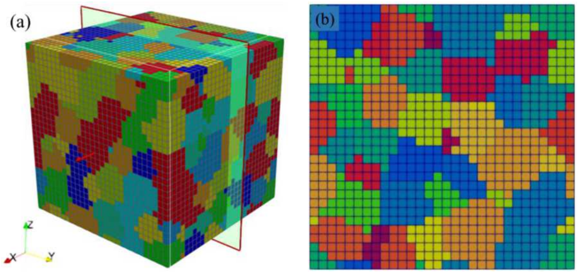

Fig. 17. The position of RVE section (a). The grain shape of the selected region (b).

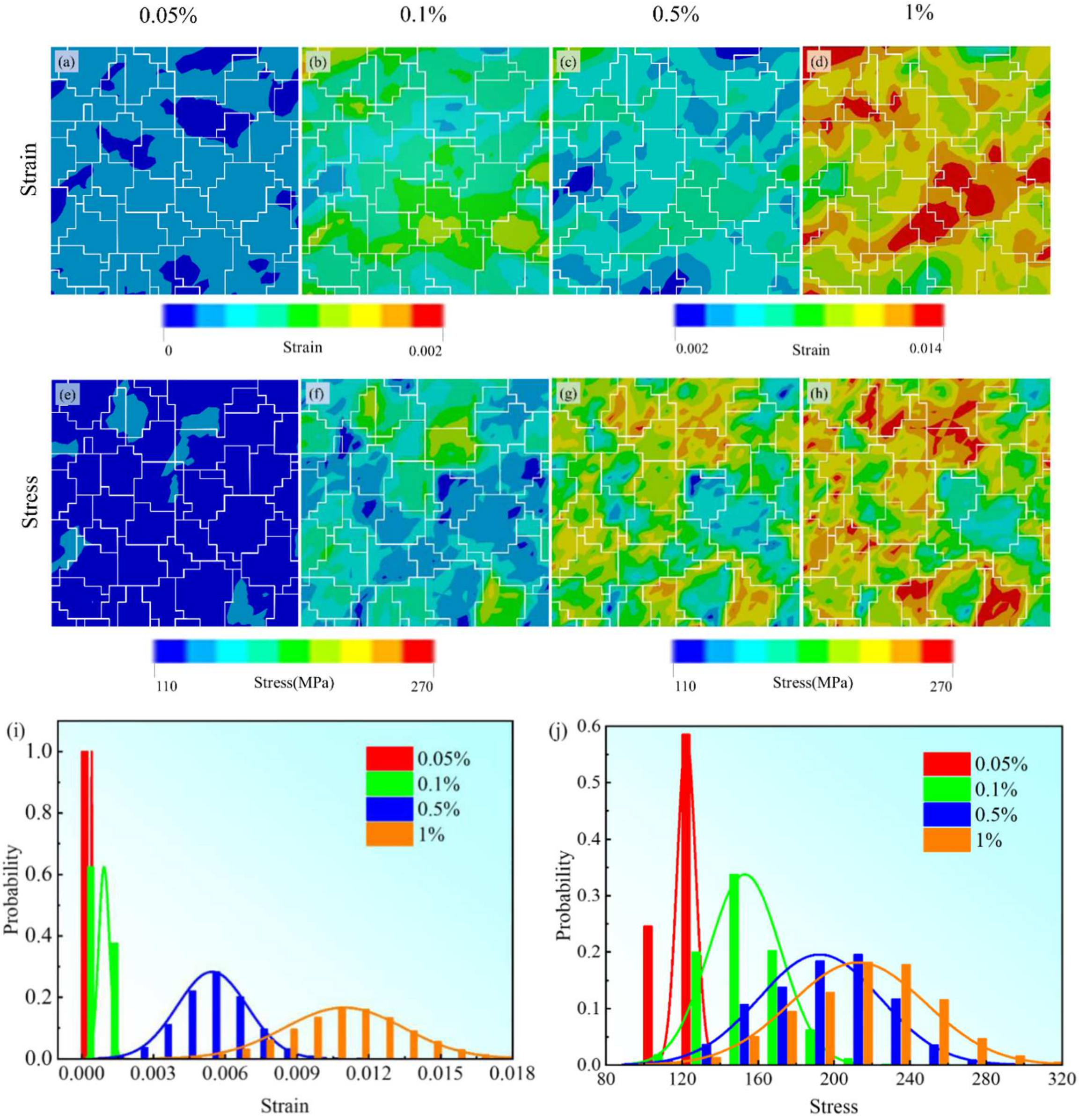

Fig. 18. The strain distribution for the elastic stage at the strain of 0.05% (a), the yielding stage at the strain of 0.1% (b), and the strain-hardening stage at the strain of 0.5% and 1% (c, d). The stress distribution for the elastic stage at the strain of 0.05% (e), the yielding stage at the strain of 0.1% (f), and the strain-hardening stage at the strain of 0.5% and 1% (g, h). For different strain stages, the probability statistics of stress and strain distribution (i, j).

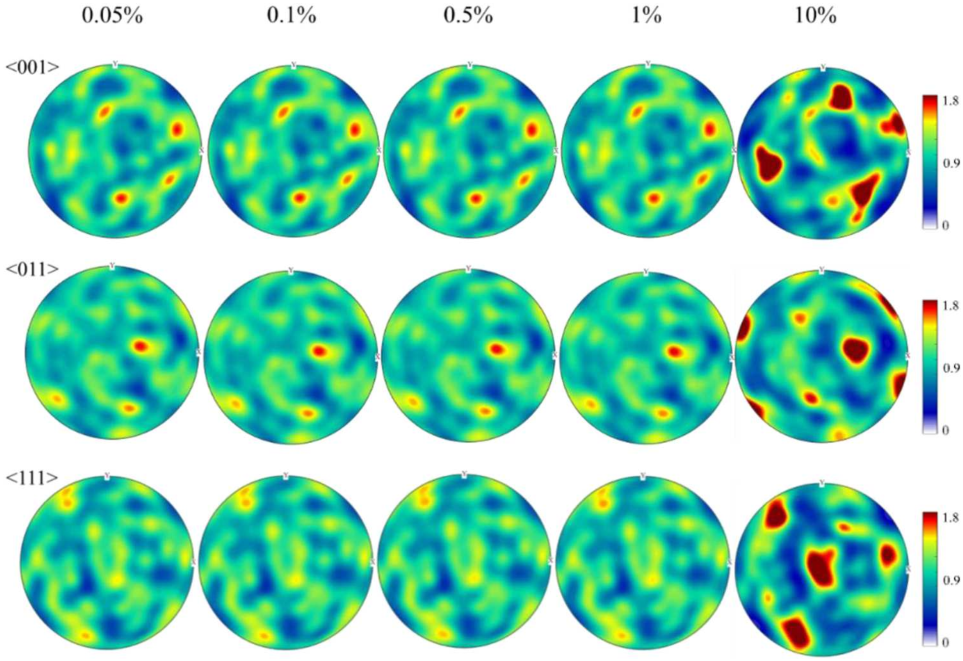

Fig. 19. The comparison of pole figures with the increasing uniaxial tension strain of 0.05%, 0.1%, 0.5%, 1%, and 10%.

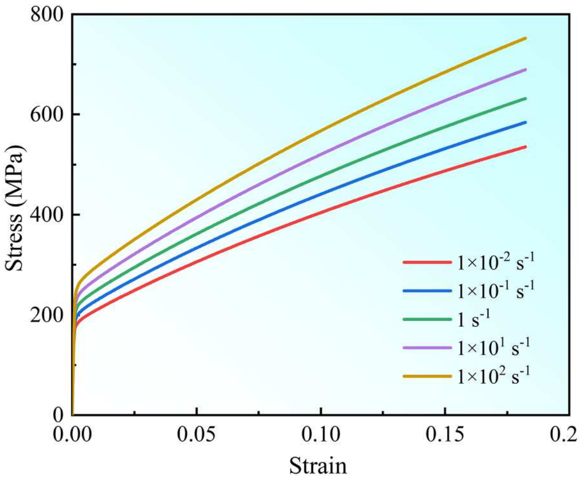

Fig. 20. The predicted strain-stress curves of the polycrystals for different strain rates.

is added to the DDD simulations of the single crystals with different crystal orientations to quantify the interactions between the dislocation and lattice distortion on the dislocation motion. The dislocation collective behavior parameters with the lattice distortion are matched with the hardening parameters of a crystal plasticity model based on the slip, and the hardening parameters of the single crystals are obtained to predict the mechanical behavior of the single crystal $Al_{0.1}$FeCoCrNi MPEA under the uniaxial tensile loading. The hardening parameter sets of the polycrystals are obtained by statistically averaging the seven calibrated single crystal hardening parameters. The CPEM simulation results show that the $Al_{0.1}$FeCoCrNi MPEA model established can accurately predict the mechanical response of the polycrystal RVE on the mesoscale. The newly developed method provides an insight into deeply understanding of the microscale deformation mechanisms related to the nano-micron-meso-scale structure, and gives some possibilities and avenues to investigate the superior mechanical properties associated with the regulation of multiscale microstructures for the advanced MPEAs.

CRediT authorship contribution statement

Qihong Fang: Conceptualization, Methodology, Software, Data curation, Writing – original draft, Funding acquisition,

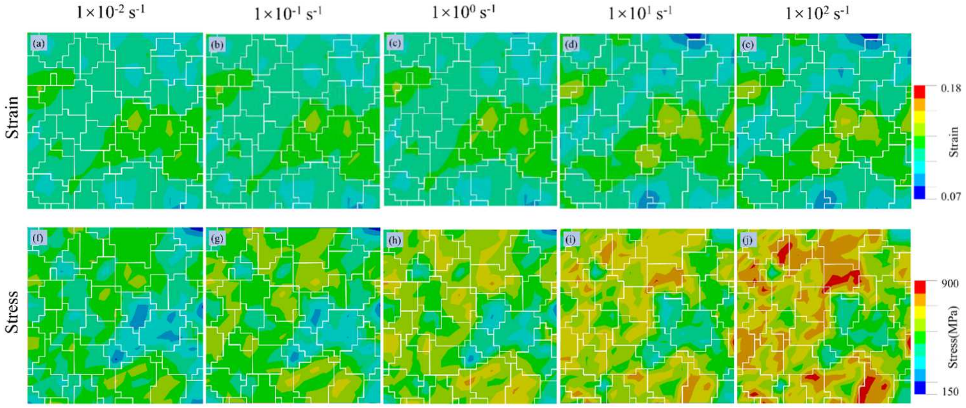

Fig. 21. The strain and stress distributions at the strain of 10% for the strain rates of 1 × 10^{-2} s^{-1}, 1 × 10^{-1} s^{-1}, 1 × 10^{0} s^{-1}, 1 × 10^{1} s^{-1}, and 1 × 10^{2} s^{-1}.

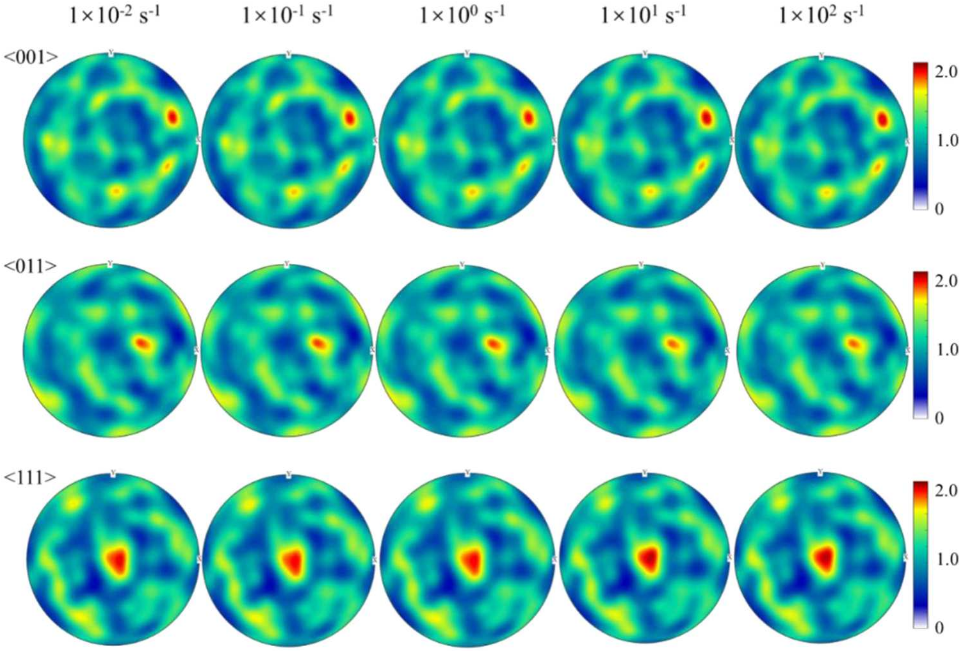

Fig. 22. The comparison of the pole figures with the increased uniaxial tension strain rates of 1 × 10^{-2} s^{-1}, 1 × 10^{-1} s^{-1}, 1 × 10^{0} s^{-1}, 1 × 10^{1} s^{-1}, and 1 × 10^{2} s^{-1} at the strain of 10%.

Investigation, Writing – review & editing, Supervision. **Weizheng Lu:** Conceptualization, Methodology, Software, Data curation, Writing – original draft, Visualization, Investigation, Writing – review & editing. **Yang Chen:** Methodology, Software, Data curation, Writing – original draft, Visualization, Investigation, Writing – review & editing. **Hui Feng:** Funding acquisition, Writing – original draft, Visualization, Investigation, Writing – review & editing. **Peter K Liaw:** Funding acquisition, Writing – original draft, Visualization, Investigation, Writing – review & editing. **Jia Li:** Conceptualization, Methodology, Software, Funding acquisition, Data curation, Writing – original draft, Visualization, Investigation, Writing – review & editing, Supervision.

Declaration of Competing Interest

The authors declare that they have no known competing financial interests or personal relationships that could have appeared to influence the work reported in this paper.

Data availability

Data will be made available on request.

Acknowledgments

The authors would like to deeply appreciate the supports from Foundation for National Natural Science Foundation of China (12172123 and 12072109), and Natural Science Foundation of Hunan Province (2022JJ20001 and 2021JJ40032). PKL very much appreciates the support from the National Science Foundation (DMR-1611180 and 1809640) and the Army Office of Research (W911NF-13-1-0438 and W911NF-19-2-0049).

References

Ahrens, J., Geveci, B., Law, C., 2005. Paraview: an end-user tool for large data visualizationHansen, C.D., Johnson, C.R. (Eds.), In: The Visualization Handbook. Elsevier, pp. 717–731.

Alleman, C., Luscher, D.J., Bronkhorst, C., Ghosh, S., 2015. Distribution-enhanced homogenization framework and model for heterogeneous elasto-plastic problems. J. Mech. Phys. Solids 85, 176–202.

Anand, L., Kothari, M., 1996. A computational procedure for rate-independent crystal plasticity. J. Mech. Phys. Solids 44, 525–558.

Arsenlis, A., Cai, W., Tang, M., Rhee, M., Oppelstrup, T., Hommes, G., Pierce, T.G., Bulatov, V.V., 2006. Enabling strain hardening simulations with dislocation dynamics. Model. Simul. Mater. Sc. 15, 553.

Arsenlis, A., Rhee, M., Hommes, G., Cook, R., Marian, J., 2012. A dislocation dynamics study of the transition from homogeneous to heterogeneous deformation in irradiated body-centered cubic iron. Acta Mater. 60, 3748–3757.

Asaro, R.J., Needleman, A., 1985. Overview no. 42 texture development and strain hardening in rate dependent polycrystals. Acta Metall. 33, 923–953.

Ausloos, M., Berman, D.H., 1985. A multivariate Weierstrass–Mandelbrot function. Proc. R. Soc. Lond. A 400, 331–350.

Bahramyan, M., Mousavian, R.T., Brabazon, D., 2020. Determination of atomic-scale structure and compressive behavior of solidified AlxCrCoFeCuNi high entropy alloys. Int. J. Mech. Sci. 171, 105389.

Balasubramanian, S., Anand, L., 2002. Elasto-viscoplastic constitutive equations for polycrystalline fcc materials at low homologous temperatures. J. Mech. Phys. Solids 50, 101–126.

Bandyopadhyay, R., Prithivirajan, V., Peralta, A.D., Sangid, M.D., 2020. Microstructure-sensitive critical plastic strain energy density criterion for fatigue life prediction across various loading regimes. Proc. Roy. Soc. A 476, 20190766.

Bangerth, W., Hartmann, R., Kanschat, G., 2007. deal. II—a general-purpose object-oriented finite element library. ACM Trans. Math. Softw. 33, 24–27.

Baudoin, P., Hama, T., Takuda, H., 2019. Influence of critical resolved shear stress ratios on the response of a commercially pure titanium oligocrystal: crystal plasticity simulations and experiment. Int. J. Plast. 115, 111–131.

Brailsford, A.D., 1972. Anharmonicity contributions to dislocation drag. J. Appl. Phys. 43, 1380–1393.

Bulatov, V.V., Hsuing, L.L., Tang, M., Arsenlis, A., Bartlet, M.C., Cai, W., Florando, J.N., Hiratani, M., Rhee, M., Hommes, G., Pierce, T.G., Diaz de la Rubia, T., 2006. Dislocation multi-junctions and strain hardening. Nature 440, 1174–1178.

Cai, W., Bulatov, V.V., Chang, J., Li, J., Yip, S., 2004. Dislocation core effects on mobility. In: Dislocations in Solids, 12. Elsevier, Ch, pp. 1–80.

Cantor, B., Chang, I.T.H., Knight, P., Vincent, A.J.B., 2004. Microstructural development in equiatomic multicomponent alloys. Mater. Sci. Eng. A 375, 213–218.

Chakraborty, S., Ghosh, S., 2021. A concurrent atomistic-crystal plasticity multiscale model for crack propagation in crystalline metallic materials. Comput. Methods Appl. Mech. Eng. 379, 113748.

Chandra, S., Samal, M.K., Chavan, V.M., Patel, R.J., 2015. Multiscale modeling of plasticity in a copper single crystal deformed at high strain rates. Plast. Mech. Defects 1, 1–16.

Chandra, S., Samal, M.K., Chavan, V.M., Raghunathan, S., 2018. Hierarchical multiscale modeling of plasticity in copper: from single crystals to polycrystalline aggregates. Int. J. Plast. 101, 188–212.

Cho, J., Molinari, J.F., Anciaux, G., 2016. Mobility law of dislocations with several character angles and temperatures in FCC aluminum. Int. J. Plast. 90, 66–75.

Choudhuri, D., Komarasamy, M., Ageh, V., Mishra, R.S., 2018. Investigation of plastic deformation modes in $Al_{0.1}$CoCrFeNi high entropy alloy. Mater. Chem. Phys. 217, 308–314.

Davydov, D., Pelteret, J.P., Steinmann, P., 2014. Comparison of several staggered atomistic-to-continuum concurrent coupling strategies. Comput. Methods Appl. Mech. Eng. 277, 260–280.

Deka, D., Joseph, D.S., Ghosh, S., Mills, M.J., 2006. Crystal plasticity modeling of deformation and creep in polycrystalline Ti-6242. Metall. Mater. Trans. A 37, 1371–1388.

Devincre, B., Kubin, L., Hoc, T., 2006. Physical analyses of crystal plasticity by DD simulations. Scr. Mater. 54, 741–746.

Dimiduk, D.M., Uchic, M.D., Parthasarathy, T.A., 2005. Size-affected single-slip behavior of pure nickel microcrystals. Acta Mater. 53, 4065–4077.

Ding, Q., Fu, X., Chen, D., Bei, H., Gludovatz, B., Li, J., Zhang, Z., George, E.P., Yu, Q., Zhu, T., Ritchie, R.O., 2019. Real-time nanoscale observation of deformation mechanisms in CrCoNi-based medium-to high-entropy alloys at cryogenic temperatures. Mater. Today 25, 21–27.

Essmann, U., Mughrabi, H., 1979. Annihilation of dislocations during tensile and cyclic deformation and limits of dislocation densities. Philos. Mag. A 40, 731–756.

Fan, H., Wang, Q., El-Awady, J.A., Raabe, D., Zaiser, M., 2021. Strain rate dependency of dislocation plasticity. Nat. Commun. 12, 1–11.

Fang, Q., Chen, Y., Li, J., Jiang, C., Liu, B., Liu, Y., Liaw, P.K., 2019. Probing the phase transformation and dislocation evolution in dual-phase high-entropy alloys. Int. J. Plast. 114, 161–173.

Fang, Q., Peng, J., Chen, Y., Li, L., Feng, H., Li, J., Jiang, C., Liaw, P.K., 2021. Hardening behaviour in the irradiated high entropy alloy. Mech. Mater. 155, 103744.

Farkas, D., Caro, A., 2020. Model interatomic potentials for Fe–Ni–Cr–Co–Al high-entropy alloys. J. Mater. Res. 35, 3031–3040.

Fish, J., Shek, K., Pandheeradi, M., Shephard, M.S., 1997. Computational plasticity for composite structures based on mathematical homogenization: theory and practice. Comput. Methods Appl. Mech. Eng. 148, 53–73.

Fivel, M., Tabourot, L., Rauch, E., Canova, G., 1998. Identification through mesoscopic simulations of macroscopic parameters of physically based constitutive equations for the plastic behaviour of fcc single crystats. J. Phys. IV France 8, 151-158.

Ganesan, S., Yaghoobi, M., Githens, A., Chen, Z., Daly, S., Allison, J.E., Sundararaghavan, V., 2021. The effects of heat treatment on the response of WE43 Mg alloy: crystal plasticity finite element simulation and SEM-DIC experiment. Int. J. Plast. 137, 102917.

Gangireddy, S., Kaimiao, L., Gwalani, B., Mishra, R., 2018. Microstructural dependence of strain rate sensitivity in thermomechanically processed $Al_{0.1}$CoCrFeNi high entropy alloy. Mater. Sci. Eng. A 727, 148–159.

Gangireddy, S., Whitaker, D., Mishra, R.S., 2019. Significant contribution to strength enhancement from deformation twins in thermomechanically processed $Al_{0.1}$CoCrFeNi microstructures. J. Mater. Eng. Perform. 28, 1661–1667.

Ghosh, S., Bai, J., Paquet, D., 2009. Homogenization-based continuum plasticity-damage model for ductile failure of materials containing heterogeneities. J. Mech. Phys. Solids 57, 1017–1044.

Ghosh, S., Bai, J., Raghavan, P., 2007. Concurrent multi-level model for damage evolution in microstructurally debonding composites. Mech. Mater. 39, 241–266.

Gludovatz, B., Hohenwarter, A., Catoor, D., Chang, E.H., George, E.P., Ritchie, R.O., 2014. A fracture-resistant high-entropy alloy for cryogenic applications. Science 345, 1153–1158.

Gnäupel-Herold, T., Brand, P.C., Prask, H.J., 1998. Calculation of single-crystal elastic constants for cubic crystal symmetry from powder diffraction data. J. Appl. Crystallogr. 31, 929–935.

Groeber, M.A., Jackson, M.A., 2014. DREAM. 3D: a digital representation environment for the analysis of microstructure in 3D. Integr. Mater. Manuf. Innov. 3, 56–72.

Groh, S., Marin, E.B., Horstemeyer, M.F., Zbib, H.M., 2009. Multiscale modeling of the plasticity in an aluminum single crystal. Int. J. Plast. 25, 1456–1473.

Hansen, N., Huang, X., 1998. Microstructure and flow stress of polycrystals and single crystals. Acta Mater. 46, 1827–1836.

Hemphill, M.A., Yuan, T., Wang, G.Y., Yeh, J.W., Tsai, C.W., Chuang, A., Liaw, P.K., 2012. Fatigue behavior of $Al_{0.5}$CoCrCuFeNi high entropy alloys. Acta Mater. 60, 5723–5734.

Huang, R., Zhang, Q., Zhang, X., Li, J., Cao, T., Yao, J., Xue, Y., Gao, H., Li, X., 2021. Dynamic recrystallization-induced temperature insensitivity of yield stress in single-crystal $Al_{1.2}$CrFeCoNi micropillars. Sci. China Technol. Sci. 64, 11–22.

Huang, S., Huang, H., Li, W., Kim, D., Lu, S., Li, X., Holmström, E., Kwon, S.K., Vitos, L., 2018. Twinning in metastable high-entropy alloys. Nat. Commun. 9, 1–7.

Hussein, A.M., Rao, S.I., Uchic, M.D., Dimiduk, D.M., El-Awady, J.A., 2015. Microstructurally based cross-slip mechanisms and their effects on dislocation microstructure evolution in fcc crystals. Acta Mater. 85, 180–190.

Jarvis, E.A.A., Hayes, R.L., Carter, E.A., 2001. Effects of oxidation on the nanoscale mechanisms of crack formation in aluminum. Chem. Phys. Chem. 2, 55–59.

Jiang, K., Ren, T., Shan, G., Ye, T., Chen, L., Wang, C., Zhao, F., Li, J., Suo, T., 2020. Dynamic mechanical responses of the $Al_{0.1}$CoCrFeNi high entropy alloy at cryogenic temperature. Mater. Sci. Eng. A 797, 140125.

Jiao, Q., Sim, G.D., Komarasamy, M., Mishra, R.S., Liaw, P.K., El-Awady, J.A., 2018. Thermo-mechanical response of single-phase face-centered-cubic AlxCoCrFeNi high-entropy alloy microcrystals. Mater. Res. Lett. 6, 300–306.

Jo, Y.H., Jung, S., Choi, W.M., Sohn, S.S., Kim, H.S., Lee, B.J., Kim, N.J., Lee, S., 2017. Cryogenic strength improvement by utilizing room-temperature deformation twinning in a partially recrystallized VCrMnFeCoNi high-entropy alloy. Nat. Commun. 8, 1–8.

Joseph, J., Stanford, N., Hodgson, P., Fabijanic, D.M., 2017. Understanding the mechanical behaviour and the large strength/ductility differences between FCC and BCC AlxCoCrFeNi high entropy alloys. J. Alloy Compd. 726, 885–895.

Kalidindi, S.R., 1992. Polycrystal plasticity: constitutive modeling and deformation processing. Ph.D. Thesis, Massachusetts Institute of Technology.

Kalidindi, S.R., 2001. Modeling anisotropic strain hardening and deformation textures in low stacking fault energy fcc metals. Int. J. Plast. 17, 837–860.

Kawamura, M., Asakura, M., Okamoto, N.L., Kishida, K., Inui, H., George, E.P., 2021. Plastic deformation of single crystals of the equiatomic Cr−Mn−Fe−Co−Ni high-entropy alloy in tension and compression from 10 K to 1273 K. Acta Mater. 203, 116454.

Kim, W.K., Luskin, M., Perez, D., Voter, A.F., Tadmor, E.B., 2014. Hyper-QC: an accelerated finite-temperature quasicontinuum method using hyperdynamics. J. Mech. Phys. Solids 63, 94–112.

Kim, Y., Asghari-Rad, P., Lee, J., Gu, G.H., Jang, M., Bouaziz, O., Estrin, Y., Kato, H., Kim, H.S., 2022. Solid solution induced back-stress in multi-principal element alloys: experiment and modeling. Mater. Sci. Eng. A 835, 142621.

Kireeva, I.V., Chumlyakov, Y.I., Vyrodova, A.V., Pobedennaya, Z.V., Karaman, I., 2020. Effect of twinning on the orientation dependence of mechanical behaviour and fracture in single crystals of the equiatomic CoCrFeMnNi high-entropy alloy at 77K. Mater. Sci. Eng. A 784, 139315.

Knezevic, M., Drach, B., Ardeljan, M., Beyerlein, I.J., 2014. Three dimensional predictions of grain scale plasticity and grain boundaries using crystal plasticity finite element models. Comput. Methods Appl. Mech. Eng. 277, 239–259.

Kotha, S., Ozturk, D., Ghosh, S., 2020. Uncertainty-quantified parametrically homogenized constitutive models (UQ-PHCMs) for dual-phase α/β titanium alloys. NPJ Comput. Mater. 6, 1–20.

Kouznetsova, V., Geers, M.G.D., Brekelmans, W.A.M., 2002. Multi-scale constitutive modelling of heterogeneous materials with a gradient-enhanced computational homogenization scheme. Int. J. Numer. Methods Eng. 54, 1235–1260.

Kulkarni, Y., Knap, J., Ortiz, M., 2008. A variational approach to coarse graining of equilibrium and non-equilibrium atomistic description at finite temperature. J. Mech. Phys. Solids 56, 1417–1449.

Kuykendall, W.P., Wang, Y., Cai, W., 2020. Stress effects on the energy barrier and mechanisms of cross-slip in FCC nickel. J. Mech. Phys. Solids 144, 104105.

Lakshmanan, A., Yaghoobi, M., Stopka, K.S., Sundararaghavan, V., 2022. Crystal plasticity finite element modeling of grain size and morphology effects on yield strength and extreme value fatigue response. J. Mater. Sci. Technol. 19, 3337–3354.

Lehtinen, A., Laurson, L., Granberg, F., Nordlund, K., Alava, M.J., 2018. Effects of precipitates and dislocation loops on the yield stress of irradiated iron. Sci. Rep. 8, 1–12.

Li, L., Fang, Q., Li, J., Liu, B., Liu, Y., Liaw, P.K., 2020. Lattice-distortion dependent yield strength in high entropy alloys. Mater. Sci. Eng. A 784, 139323.

Li, J., Chen, Y., He, Q., Xu, X., Wang, H., Jiang, C., Liu, B., Fang, Q., Liu, Y., Yang, Y., 2022. Heterogeneous lattice strain strengthening in severely distorted crystalline solids. Proc. Natl. Acad. Sci. USA 119, e2200607119.

Li, J., Fang, Q., Liu, B., Liu, Y., Liu, Y., 2016. Mechanical behaviors of AlCrFeCuNi high-entropy alloys under uniaxial tension via molecular dynamics simulation. RSC Adv. 6, 76409–76419.

Li, J., Chen, H.T., Fang, Q.H., Jiang, C., Liu, Y., Liaw, P.K., 2020. Unraveling the dislocation-precipitate interactions in high-entropy alloys. Int. J. Plast. 133, 102819.

Li, S., 2008. Orientation stability in equal channel angular extrusion. Part II: Hexagonal close-packed materials. Acta Mater. 56, 1031–1043.

Li, W., Chen, S., Liaw, P.K., 2020. Discovery and design of fatigue-resistant high-entropy alloys. Scr. Mater. 187, 68–75.

Li, W.D., Liaw, P.K., Gao, Y.F., 2018. Fracture resistance of high entropy alloys: a review. Intermetallics 99, 69–83.

Li, Y., Zhu, L., Liu, Y., Wei, Y., Wu, Y., Tang, D., Mi, Z., 2013. On the strain hardening and texture evolution in high manganese steels: experiments and numerical investigation. J. Mech. Phys. Solids 61, 2588–2604.

Liang, Y.J., Wang, L., Wen, Y., Cheng, B., Wu, Q., Cao, T., Xiao, Q., Xue, Y., Sha, G., Wang, Y.D., Ren, Y., Li, X.Y., Wang, L., Wang, C.F., Cai, H.N., 2018. High-content ductile coherent nanoprecipitates achieve ultrastrong high-entropy alloys. Nat. Commun. 9, 1–8.

Lu, P., Zhang, T.W., Zhao, D., Ma, S.G., Li, Q., Wang, T., Wang, Z.H., 2021. Effects of stress states and strain rates on mechanical behavior and texture evolution of the CoCrFeNi high-entropy alloy: experiment and simulation. J. Alloys Compd. 851, 156779.

Lu, S., Zhang, B., Li, X., Zhao, J., Zaiser, M., Fan, H., Zhang, X., 2019. Grain boundary effect on nanoindentation: a multiscale discrete dislocation dynamics model. J. Mech. Phys. Solids 126, 117–135.

Lu, X., Zhao, J., Yu, C., Li, Z., Kan, Q., Kang, G., Zhang, X., 2020. Cyclic plasticity of an interstitial high-entropy alloy: experiments, crystal plasticity modeling, and simulations. J. Mech. Phys. Solids 142, 103971.

Madec, R., 2001. Dislocation interactions to plastic flow in fcc single crystals: a study by simulation of dislocation dynamics. Ph.D. Thesis, Orsay University.

Massart, T.J., Peerlings, R.H.J., Geers, M.G.D., 2007. Structural damage analysis of masonry walls using computational homogenization. Int. J. Damage Mech. 16, 199–226.

McGinty, R.D., McDowell, D.L., 2004. Application of multiscale crystal plasticity models to forming limit diagrams. J. Eng. Mater. Technol. 126, 285–291.

Mecking, H., Kocks, U.F., 1981. Kinetics of flow and strain-hardening. Acta Metall. 29, 1865–1875.

Meyers, M.A., 1994. Dynamic Behavior of Materials. John Wiley & Sons, New York.

Miller, R.E., Shilkrot, L.E., Curtin, W.A., 2004. A coupled atomistics and discrete dislocation plasticity simulation of nanoindentation into single crystal thin films. Acta Mater. 52, 271–284.

Miracle, D.B., Senkov, O.N., 2017. A critical review of high entropy alloys and related concepts. Acta Mater. 122, 448–511.

Moon, J., Jang, M.J., Bae, J.W., Yim, D., Park, J.M., Lee, J., Kim, H.S., 2018. Mechanical behavior and solid solution strengthening model for face-centered cubic single crystalline and polycrystalline high-entropy alloys. Intermetallics 98, 89–94.

Norfleet, D.M., Dimiduk, D.M., Polasik, S.J., Uchic, M.D., Mills, M.J., 2008. Dislocation structures and their relationship to strength in deformed nickel microcrystals. Acta Mater. 56, 2988–3001.

Olmsted, D.L., Hector, L.G., Curtin, W.A., Clifton, R.J., 2005. Atomistic simulations of dislocation mobility in Al, Ni and Al/Mg alloys. Model. Simul. Mater. Sci. Eng. 13, 371.

Ortiz, M., Phillips, R., 1998. Nanomechanics of defects in solids. Adv. Appl. Mech. 36, 1–79.

Otto, F., Dlouhý, A., Somsen, C., Bei, H., Eggeler, G., George, E.P., 2013. The influences of temperature and microstructure on the tensile properties of a CoCrFeMnNi high-entropy alloy. Acta Mater. 61, 5743–5755.

Ozturk, D., Kotha, S., Ghosh, S., 2021. An uncertainty quantification framework for multiscale parametrically homogenized constitutive models (PHCMs) of polycrystalline Ti alloys. J. Mech. Phys. Solids 148, 104294.

Ozturk, D., Kotha, S., Pilchak, A.L., Ghosh, S., 2019. Two-way multi-scaling for predicting fatigue crack nucleation in titanium alloys using parametrically homogenized constitutive models. J. Mech. Phys. Solids 128, 181–207.

Pan, Q., Zhang, L., Feng, R., Lu, Q., An, K., Chuang, A.C., Poplawsky, J.D., Liaw, P.K., Lu, L., 2021. Gradient cell–structured high-entropy alloy with exceptional strength and ductility. Science 374, 984–989.

Park, J.M., Moon, J., Bae, J.W., Jang, M.J., Park, J., Lee, S., Kim, H.S., 2018. Strain rate effects of dynamic compressive deformation on mechanical properties and microstructure of CoCrFeMnNi high-entropy alloy. Mater. Sci. Eng. A 719, 155–163.

Peng, J., Li, L., Li, F., Liu, B., Zherebtsov, S., Fang, Q., Li, J., Stepanov, N., Liu, Y., Liu, F., 2021. The predicted rate-dependent deformation behaviour and multistage strain hardening in a model heterostructured body-centered cubic high entropy alloy. Int. J. Plast. 145, 103073.

Plimpton, S., 1995. Fast parallel algorithms for short-range molecular dynamics. J. Comput. Phys. 117, 1–19.

Po, G., Cui, Y., Rivera, D., Cereceda, D., Swinburne, T.D., Marian, J., Ghoniem, N., 2016. A phenomenological dislocation mobility law for bcc metals. Acta Mater. 119, 123–135.

Prithivirajan, V., Sangid, M.D., 2018. The role of defects and critical pore size analysis in the fatigue response of additively manufactured IN718 via crystal plasticity. Mater. Des. 150, 139–153.

Rao, S.I., Woodward, C., Akdim, B., Antillon, E., Parthasarathy, T.A., El-Awady, J.A., Dimiduk, D.M., 2019. Large-scale dislocation dynamics simulations of strain hardening of Ni microcrystals under tensile loading. Acta Mater. 164, 171–183.

Rao, S.I., Woodward, C., Parthasarathy, T.A., Senkov, O., 2017. Atomistic simulations of dislocation behavior in a model FCC multicomponent concentrated solid solution alloy. Acta Mater. 134, 188–194.

Renner, E., Gaillard, Y., Richard, F., Amiot, F., Delobelle, P., 2016. Sensitivity of the residual topography to single crystal plasticity parameters in Berkovich nanoindentation on FCC nickel. Int. J. Plast. 77, 118–140.

Roters, F., Diehl, M., Shanthraj, P., Eisenlohr, P., Reuber, C., Wong, S.L., Maiti, T., Raabe, D., 2019. DAMASK–the düsseldorf advanced material simulation kit for modeling multi-physics crystal plasticity, thermal, and damage phenomena from the single crystal up to the component scale. Comput. Mater. Sci. 158, 420–478.

Shao, Y.T., Yuan, R., Hu, Y., Yang, Q., Zuo, J.M., 2019. The paracrystalline nature of lattice distortion in a high entropy alloy. arXiv:1903.04082.

Shehadeh, M.A., 2012. Multiscale dislocation dynamics simulations of shock-induced plasticity in small volumes. Philos. Mag. 92, 1173–1197.

Shen, Y., Spearot, D.E., 2021. Mobility of dislocations in FeNiCrCoCu high entropy alloys. Model. Simul. Mater. Sci. Eng. 29, 085017.

Shenoy, V.B., Miller, R., Tadmor, E.B., Phillips, R., Ortiz, M., 1998. Quasicontinuum models of interfacial structure and deformation. Phys. Rev. Lett. 80, 742.

Shi, P., Li, R., Li, Y., Wen, Y., Zhong, Y., Ren, W., Shen, Z., Zheng, T., Peng, J., Liang, X., 2021. Hierarchical crack buffering triples ductility in eutectic herringbone high-entropy alloys. Science 373, 912–918.

Shi, Y., Yang, B., Liaw, P.K., 2017. Corrosion-resistant high-entropy alloys: a review. Metals 7, 43.

Shilkrot, L.E., Miller, R.E., Curtin, W.A., 2002. Coupled atomistic and discrete dislocation plasticity. Phys. Rev. Lett. 89, 025501.

Shukla, S., Wang, T., Cotton, S., Mishra, R.S., 2018. Hierarchical microstructure for improved fatigue properties in a eutectic high entropy alloy. Scr. Mater. 156, 105–109.

Sills, R.B., Bertin, N., Aghaei, A., Cai, W., 2018. Dislocation networks and the microstructural origin of strain hardening. Phys. Rev. Lett. 121, 085501.

Smith, L.T.W., Su, Y., Xu, S., Hunter, A., Beyerlein, I.J., 2020. The effect of local chemical ordering on Frank-Read source activation in a refractory multi-principal element alloy. Int. J. Plast. 134, 102850.

Song, D., Castañeda, P.P., 2018. A multi-scale homogenization model for fine-grained porous viscoplastic polycrystals: II–Applications to FCC and HCP materials. J. Mech. Phys. Solids 115, 77–101.

Stopka, K.S., Yaghoobi, M., Allison, J.E., McDowell, D.L., 2021. Effects of boundary conditions on microstructure-sensitive fatigue crystal plasticity analysis. Integr. Mater. Manuf. Innov. 1–20.

Stukowski, A., 2009. Visualization and analysis of atomistic simulation data with OVITO–the Open visualization tool. Model. Simul. Mater. Sci. Eng. 18, 015012.

Sundararaghavan, V., Zabaras, N., 2008. A multi-length scale sensitivity analysis for the control of texture-dependent properties in deformation processing. Int. J. Plast. 24, 1581–1605.

Thurston, K., Gludovatz, B., Hohenwarter, A., Laplanche, G., George, E.P., Ritchie, R.O., 2017. Effect of temperature on the fatigue-crack growth behavior of the high-entropy alloy CrMnFeCoNi. Intermetallics 88, 65–72.

Wang, W., Wang, W., Wang, S., Tsai, Y., Lai, C., Yeh, J., 2012. Effects of Al addition on the microstructure and mechanical property of AlxCoCrFeNi high-entropy alloys. Intermetallics 26, 44–51.

Wang, Y.U., Jin, Y.M., Cuitino, A.M., Khachaturyan, A.G., 2001. Nanoscale phase field microelasticity theory of dislocations: model and 3D simulations. Acta Mater. 49, 1847–1857.

Wang, Z., Fang, Q.H., Li, J., Liu, B., Liu, Y., 2018. Effect of lattice distortion on solid solution strengthening of BCC high-entropy alloys. J. Mater. Sci. Technol. 34, 349–354.

Wei, D., Zaiser, M., Feng, Z., Kang, G., Fan, H., Zhang, X., 2019. Effects of twin boundary orientation on plasticity of bicrystalline copper micropillars: a discrete dislocation dynamics simulation study. Acta Mater. 176, 289–296.

Wu, J., 2002. Analyses and simulation of anisotropic fractal surfaces. Chaos Solitons Fractals 13, 1791–1806.

Wu, S.W., Wang, G., Yi, J., Jia, Y.D., Hussain, I., Zhai, Q.J., Liaw, P.K., 2017. Strong grain-size effect on deformation twinning of an $Al_{0.1}$CoCrFeNi high-entropy alloy. Mater. Res. Lett. 5, 276–283.

Xiao, Y., Kuang, W., Xu, Y., Wu, L., Gong, W., Qian, J., Zhang, Q., He, Y., 2019. Microstructure and oxidation behavior of the CrMoNbTaV high-entropy alloy. J. Mater. Res. 34, 301–308.

Yaghoobi, M., Ganesan, S., Sundar, S., Lakshmanan, A., Rudraraju, S., Allison, J.E., Sundararaghavan, V., 2019. PRISMS-Plasticity: an open-source crystal plasticity finite element software. Comput. Mater. Sci. 169, 109078.

Yan, W., Komvopoulos, K., 1998. Contact analysis of elastic-plastic fractal surfaces. J. Appl. Phys. 84, 3617–3624.

Yeh, J.W., Chen, S.K., Lin, S.J., Gan, J.Y., Chin, T.S., Shun, T.T., Tsau, C.H., Chang, S.Y., 2004. Nanostructured high-entropy alloys with multiple principal elements: novel alloy design concepts and outcomes. Adv. Eng. Mater. 6, 299–303.

Yin, S., Zuo, Y., Abu-Odeh, A., Zheng, H., Li, X.G., Ding, J., Ong, S.P., Asta, M., Ritchie, R.O., 2021. Atomistic simulations of dislocation mobility in refractory high-entropy alloys and the effect of chemical short-range order. Nat. Commun. 12, 1–14.

Yu, P.F., Cheng, H., Zhang, L.J., Zhang, H., Jing, Q., Ma, M.Z., Liaw, P.K., Li, G., Liu, R.P., 2016. Effects of high pressure torsion on microstructures and properties of an $Al_{0.1}$CoCrFeNi high-entropy alloy. Mater. Sci. Eng. A 655, 283–291.

Zecevic, M., Knezevic, M., 2018. Latent hardening within the elasto-plastic self-consistent polycrystal homogenization to enable the prediction of anisotropy of AA6022-T4 sheets. Int. J. Plast. 105, 141–163.

Zeng, Z., Li, X., Xu, D., Lu, L., Gao, H., Zhu, T., 2016. Gradient plasticity in gradient nano-grained metals. Extreme Mech. Lett. 8, 213–219.

Zhang, Q., Huang, R., Zhang, X., Cao, T., Xue, Y., Li, X., 2021. Deformation mechanisms and remarkable strain hardening in single-crystalline high-entropy-alloy micropillars/nanopillars. Nano Lett. 21, 3671–3679.

Zhang, Q., Huang, R., Jiang, J., Cao, T., Zeng, Y., Li, J., Xue, Y., Li, X., 2022. Size effects and plastic deformation mechanisms in single-crystalline CoCrFeNi micro/nanopillars. J. Mech. Phys. Solids 162, 104853.

Zhang, X., Lu, S., Zhang, B., Tian, X., Kan, Q., Kang, G., 2021. Dislocation–grain boundary interaction-based discrete dislocation dynamics modeling and its application to bicrystals with different misorientations. Acta Mater. 202, 88–98.

Zhang, Y., Zhou, Y.J., Lin, J.P., Chen, G.L., Liaw, P.K., 2008. Solid-solution phase formation rules for multi-component alloys. Adv. Eng. Mater. 10, 534–538.

Zhang, Y., Zuo, T.T., Tang, Z., Gao, M.C., Dahmen, K.A., Liaw, P.K., Lu, Z.P., 2014. Microstructures and properties of high-entropy alloys. Prog. Mater. Sci. 61, 1–93.

Zhang, Z., Sheng, H., Wang, Z., Gludovatz, B., Zhang, Z., George, E.P., Yu, Q., Mao, S.X., Ritchie, R.O., 2017. Dislocation mechanisms and 3D twin architectures generate exceptional strength-ductility-toughness combination in CrCoNi medium-entropy alloy. Nat. Commun. 8, 1–8.

Zhou, C., Biner, S.B., LeSar, R., 2010. Discrete dislocation dynamics simulations of plasticity at small scales. Acta Mater. 58, 1565–1577.